Application of An Integrated HPC Reliability Prediction Framework to HMMWV Suspension System

Dan M. Ghiocel
GP Technologies, Inc.
Pittsford, NY 14534

Dan Negrut
Mech. Engineering
Univ. of Wisconsin
Madison, WI

David Lamb
U.S. Army TARDEC
Warren, MI

David Gorsich
U.S. Army TARDEC
Warren, MI

ABSTRACT

This research paper addresses the ground vehicle reliability prediction process based on a new integrated reliability prediction framework. The paper is an extension of the paper presented last year at the GVSETS symposium. The integrated stochastic framework combines the computational physics-based predictions with experimental testing information for assessing vehicle reliability. The integrated reliability prediction approach incorporates the following computational steps: i) simulation of stochastic operational environment, ii) vehicle multi-body dynamics analysis, iii) stress prediction in subsystems and components, iv) stochastic progressive damage analysis, and v) component life prediction, including the effects of maintenance and, finally, iv) reliability prediction at component and system level. To solve efficiently and accurately the challenges coming from large-size computational mechanics models and high-dimensional stochastic spaces, a HPC simulation-based approach to the reliability problem was implemented. The integrated HPC stochastic approach combines the computational stochastic mechanics predictions with available statistical experimental databases for assessing vehicle system reliability. The paper illustrates the application of the integrated approach to evaluate the relliability of the HMMWV front-left suspension system.

DISCLAIMER: The HMMWV dynamic model and the suspension system configuration used in this research are slightly different than the actual HMMWV hardware. Thus, the presented results do not reflect in detail the real HMMWV suspension system behavior. The intent of the paper is to discuss the integrated reliability methodology and to highlight qualitative aspects.

INTRODUCTION

An aspect of a key importance for accurate reliability prediction is the integration of various types of uncertain information sources and the incorporation of the lack of data effects. If modeling uncertainties are included, the stochastic dimensionality of the vehicle reliability problem increases from a single stochastic model to a set of stochastic prediction models that correspond to the stochastic model space. It should be noted that stochastic model space is usually a high-dimensional parameter space since it includes various model parameters that are considered random quantities. A flowchart of the computational reliability prediction process is shown in Figure 1 [3]. The paper focuses on the two upper-left blocks of the reliability chart that are drawn with dotted lines, that incorporate stochastic modeling and simulation of i) road profiles and ii) vehicle system dynamic behavior. However, for reader's clarity, we briefly discuss other important aspects of the vehicle reliability prediction. The two lower-level blocks called "TAO RBDO" that are a specific part of the reliability-based optimization process using the TAO software developed by Argonne National Lab that is not addressed in this paper.

The HMMWV suspension reliability analysis consisted in the following steps:

1) Simulate stochastic road profile variations. The idealization of road profiles includes the superposition of two stochastic variations: i) the road surface variation (micro-scale continuous, including smooth variations and random bumps

or holes), and ii) the road topography variation (macro-scale continuous variations, including curves and slopes).

2) Simulate the HMMWV suspension parameters using randomly distributed variables to modify the nominal values. Average vehicle speed was varied between 17 MPH and 30 MPH.

3) Perform multibody dynamics simulations of the HMMWV system using as stochastic inputs the road profiles and vehicle suspension dynamic parameters (stiffness, damping). For each simulated road profile, a vehicle multibody dynamics analysis was run to get simulated forces and displacements at each joint of the suspension system.

4) Perform finite element (FE) stress analysis of the selected subsystem. From each HMMWV dynamics simulation a number of local response variables were considerd as random inputs for the stochastic FE stress analysis of the Front-Left Suspension System (FLSS). An efficient high-performance computing (HPC) stochastic finite-element analysis (FEA) code is employed.

5) Compute the local stresses refined using stochastic response surface approximation (SRSA) models. These SRSA models are based on high-order stochastic field models that are capable of handling non-Gaussian variations, and non-linear correlations between component variables.

6) Perform durability analysis under random corrosion-fatigue damage using stochastic crack nucleation and crack propagation models based on the damage curve approach (DCA) and the modified Forman crack propagation models. For reliability prediction at each critical location, probabilistic models based on lognormal and Weibull distributions were applied.

7) Incorporate the uncertainty effects due to the lack of data.

8) Incorporate Bayesian updating models for including experimental evidence form test data (for stresses) and field data (field failures).

The paper provides in next sections more details on the reliability prediction methodology and, also, illustrates HMMWV sensitivity analysis results. It should be noted that the presented results are based on a “modified” HMMWV vehicle model developed based on incomplete, limited information [2].

OPERATIONAL ENVIRONMENT

This section briefly describes the stochastic models used for the simulation of the road profiles.

The idealization of road profiles includes the superposition of two stochastic variations: i) the road surface variation (micro-scale continuous, including smooth variations and random bumps or holes), and ii) the road topography variation (macro-scale continuous variations, including curves and slopes).

Vehicle suspension parameters were varied by using randomly distributed variables to modify the nominal values. Average vehicle speeds were varied between 17 MPH and 30 MPH for moderate roughness roads (road surface amplitude up to 0.5 ft above mean surface) and limited to 17 mph for high rounghness roads (road surface amplitude up to 0.5-1.0 ft above mean surface). Simulations were run using random combinations of the above mentioned variations.

Specifically, we idealized the road surface profiles as non-Gaussian, non-stationary vector-valued stochastic field models with complex spatial correlation structures. To simulate stochastic road profiles, we used two approaches: i) a stochastic field approach based on application of second-order cascaded filtered Gaussian white-noise processes and ii) stochastic field approach based on the Fourier convolution of the road profile with correlated Gaussian white-noise processes. We idealized the road profiles with non-Gaussian, non-stationary Markov vector processes. To handle non-Gaussianity variation aspects we used translation processes, i.e. applied a probability

transformation of the real, non-Gaussian variations of the road surfaces and topography to virtual Gaussian spaces.

Figure 2 shows simulated road surface segments with high spatial correlation (HC) and low spatial correlation (LC) in the transverse direction of the road. The longitudinal variation of the mid-line road surface profile is the same for both HC and LC simulated roads. The HC road corresponds to a situation when the wheel inputs are about the same for two parallel wheel lines, so that right-side and left-side wheels see about the same road surface track lines. Thus, for the HC roads, there two different wheel road inputs, each input for a pair of front-rear wheels. In contrast, the LC road assumes that the right-side and left-side wheel road inputs are different. Thus, for LC roads there are four different wheel inputs. Thus, it is expected that a LC road profile will produce slighly larger vehicle dynamic responses in all directions, especially in the lateral direction.

Based on various road measurements we noted that the road surface variations are highly non-Gaussian as shown in Figure 3. This is somehow surprising since in the current practice the road surface profiles have been always idealized by simple zero-mean Gaussian stationary stochastic processes. For Gaussian stochastic processes, the covariance function (CF), or, alternatively, the power spectral density function (PSD, fully describes the stochastic process variation. In practice, the RMS value (standard deviation) and the PSD estimate are often used. Unfortunately, the RMS and PSD estimates are not sufficient for describing the non-Gaussian road surface variations. Most of the times, the road surface variations are highly non-Gaussian variations with a highly skewed probability density function (PDF) as indicated in Figure 3. The non-Gaussian variation aspect has a significant impact on the vehicle fatigue reliability prediction. It should be noted that if the non-Gaussian variation aspects of road surfaces are neglected, then, the predicted vehicle fatigue life and reliability are much larger than in reality.

Figure 4 shows simulated non-Gaussian stochastic road surface profiles (median line) with different road roughnesses and no topography included. These segments correspond to limited-size stationary segments of the road profiles.

VEHICLE DYNAMIC MODEL

Specifically, in this project the HMMWV model number M966 (TOW Missle Carrier, Basic Armor without weapons) was selected, since the values of the total vehicle inertia were available [2]. The HMMWV vehicle is designed for both on-road and off-road applications, and all models share a common chassis with 4x4 wheel drive that is powered by a 145-hp engine. Only the major subsystems which were included in the HMMWV dynamic model (Figure 5) including parallel link steering with a pitman arm, double A-arm suspension, chassis, roll stabilization bar, powertrain and tires. Subsystems for the brakes and wheels were also included in the multi-body dynamics model.

A double Ackerman Arm type suspension unit is used on the HMMWV, one for each wheel. Dimensions and locations of the suspension elements differ between the front and rear subsystems; however, the topology remains the same. Both upper and lower control arms are connected to the upright arm with ball joints. The upright arm connects the wheel spindle to the suspension units. Rear radius rods are connected between the chassis to the rear suspension and control the rear wheel static toe angle. Front tie rods attach the steering subsystem with the front suspension and control the wheel steer angle. Front and rear suspensions both have a design Kingpin angle of 12 degrees and a kingpin offset of 2.14 inches. The front suspension has a caster angle of 3 degrees and a caster offset of 0.857 inches. Topology of the suspension as modeled for vehicle dynamics analysis can be seen in Figure 6.

Shock absorber units are located on each suspension unit, and are attached between the lower control arm and chassis. Each shock absorber is comprised of three elements: a spring, a damper and a bumpstop. At design load and height, the springs are assumed to have linear

behavior. The dampers on the other hand are meant to provide dissipative forces and are not linear. Dissipative forces are proportional to the relative velocity between the piston and cylinder of the shock. Both front and rear springs and dampers were modeled in a similar way, but using different data. The rear springs and dampers are designed for larger operating loads. Bumpstops are located on the end of the damper and provide an additional damping force in the shocks. They are engaged only after a certain amount of displacement occurs between the piston and cylinder of the shock absorber. Spring, damper and bumpstop parameters can be found in [2].

The vehicle body is modeled as a single rigid-body component with mass-inertia properties as given in [2]. As stated earlier, both the vehicle mass-inertia properties and the masses of the individual subsystems are known. Simplified geometry like that in Figure 4 was used to calculate each subsystem's respective moment of inertia values.

Tires used for all simulations were the bias-type 36x12.5. Front tire pressures of 20 pounds per square inch (psi) and rear tire pressures of 30 psi were maintained on the HMMWV. By using FTire's template modeling scheme [1], only a select number of tire size, geometry and specification parameters were needed as input into the tire model; other characteristics such as carcass mass/damping/stiffness, tread and friction information were either inherited from the light truck tire template or could be calculated with a pre-processor routine.

A more detailed description of the HMMWV vehicle model is provided elsewhere [7].

HMMWV BEHAVIOR SIMULATION

In light of the importance of the tire/road interaction due to the stochastic modeling of the road profiles, a co-simulation environment was used to accurately capture the vehicle dynamics. A specialized code was used to simulate the multi-body dynamics of the HMMWV vehicle, and the tires and tire/road interaction are simulated by FTire. Road profiles of nearly a mile in length were used, and as such the computational model for determining the tire/road forces must be efficient and scalable.

The modeling methodology divides a vehicle in subsystems that are modeled independently. Parameters are applied to the topology of a subsystem and a set of subsystems are invoked and integrated together at simulation time to represent the vehicle model. The subsystems present in our model include: a chassis, front and rear suspension, anti-roll bar, steering, brakes, a powertrain and four wheels. Note that only the wheels and not the tires are present in the vehicle model. Also, all the major subsystems (front/rear suspension, steering, roll bar and powertrain) are connected to the chassis with bushing elements. The HMMWV model is shown in Figure 5 (chassis geometry is partially transparent). CAD geometry is applied to the chassis and tires to make the vehicle look realistic for animation purposes. The geometry has no bearing on the dynamic behavior of the vehicle.

Driver controls were created in the event builder as a sequence of maneuvers. Maneuvers are defined by steering, throttle, brake, gear, and clutch parameters. In this set of simulations, a single maneuver is performed in which the vehicle attempts to follow the centerline of the road profile at a given vehicle speed. Static set-up and gear shifting parameters are not modified; however, the drive authority is sometimes reduced when large obstacles and high vehicle speeds cause simulations to fail. Drive authority specifies how aggressively the vehicle steering torque is applied when the vehicle deviates off the specified path. As the wheelbase of the HMMWV is wide and long, the minimum preview distance was substantially increased from its default value. A number of about 500 stochastic simulations were performed assuming as stochastic inputs different road profiles and vehicle suspension parameters. Figure 7 decribes different categories of stochastic road profiles.

First, only the stochasticity associated to the road profile and vehicle speed were considered,

assuming a deterministic HMMWV model. These simulations utilized the same vehicle/tire models, and varied the operating environment by changing 1) road profiles 2) adding topology and 3) modifying the average vehicle speed. Road profiles were either 5000 feet or 1500 feet in length, with both high and low correlation variations in the transverse direction. Topology on the road included rolling hills with short chicanes, long winding curves or no topology at all (straight road). The average vehicle speed was either 17 MPH or 30 MPH.

Secondly, for selected road profiles, we considered that the HMMWV model suspension parameter variations are stochastic. Two types of simulated road profiles with and without topographic effects were employed. For each wheel suspension system there are 13 random variables. For four wheel suspensions there are 52 variables. To handle these large numbers of variables we condensed them in three stochastic variation features: 1) BUSHINGS UCA (4 variables), 2) BUSHINGS LCA (4 variables), 3) TIRE (3 variables) and 4) SPRING-SHOCK ABSORBER (2 variables).

The stochastic variables are modeled by i) lognormal variables with 2% and 5% c.o.v. for the spring and damper properties, ii) lognormal variables with 2% c.o.v. for bushing properties, iii) lognormal variables with 5% c.o.v. for tire properties. Currently, we are still reviewing technical literature to find specific statistical information for HMMWV dynamic system parameters. Any specific information on HMMWV coming from TARDEC will be highly appreciated.

To simulate the four stochastic variation features, we used Latin Hypercube Sampling (LHS) technique. Using LHS, stochastic input scenarios were created for each vehicle suspension stochastic feature. For each of the four stochastic features we have simulated a number of 80 input scenarios that we run separately.

For each simulated road profile, we performed a vehicle multibody dynamics analysis to get forces and displacements at each joint of the front suspension system. Stochastic variations in vehicle dynamic parameters (stiffness, damping) were included. From each the vehicle dynamics simulation, we saved 34 output variables with 1-3 component time-histories for various front-left suspension joint forces and displacements, vehicle chassis motion, displacements at wheel tire/road interface. A number of 36 variables were used as random inputs in the stochastic FE stress analysis of FLSS. Each joint force component was used to scale the local stress influence coefficients computed for unit forces in the joints.

SUSPENSION SYSTEM STRESS ANALYSIS

The stochastic subsystem stress analysis is based on an efficient high-performance computing (HPC) stochastic finite-element analysis (FEA) code developed by GP Technologies. Figure 8 shows the FLSS model used for the HMMWV vehicle multi-body dynamics analysis and the stochastic FEA.

The stochastic FEA code is a result of integrating a finite element with a number of modules used for stochastic modeling and simulation that run together in an efficient computing environment driven by advanced HPC numerical libraries available from national labs and top universities. In addition to the standard FEA and HPC algorithms, the developed code includes a unique suite of computational tools for stochastic modeling and simulation and stochastic preconditioning [3].

For stochastic FEA domain decomposition we used an efficient multilevel partitioner software. Multilevel partitioners rely on the notion of restricting the fine graph to a much smaller coarse graph, by using maximal independent set or maximal matching algorithms. This process is applied recursively until the graph is small enough that a high quality partitioner, such as spectral bisection or k-way partitioners, can be applied. This partitioning of the coarse problem is then “interpolated” back to the finer graph – a local “smoothing” procedure is then used, at each

level, to locally improve the partitioning. These methods are poly-logarithmic in complexity though they have the advantage that they can produce more refined partitions and more easily accommodate vertex and edge weights in the graph.

The main idea to build a flexible HPC implementation structure for stochastic parallel FEA has been to combine the parallel decomposition in the simulated sample data space with the parallel decomposition in the physical-model space. This combination of parallel data space decomposition with parallel physical space decomposition provides a very high numerical efficiency for handling large-size stochastic FE models. This HPC strategy provides an optimal approach for running large-size stochastic FE models. We called this HPC implementation is called the Controlled Domain Decomposition (CDD) strategy. The CDD strategy can be applied for handling multiple FE models with different sizes that will be split on a different number of processors as shown Figure 9.

There is an optimum number of processors to be used for each FE model, so that the stochastic parallel FEA reaches the best scalability. The main advantage of the CDD implementation for HPC FEA is that large-size FE models can be partitioned into a number of FE submodels, each being solved on a single processor. Thus, each group of processors is dedicated to solve a large-size FE model. CDD ensures dynamic load balancing after a group of processors has completed its allocated tasks and it becomes available for helping another group of processors.

To be highly efficient for large-size FEA models, the stochastic FEA code incorporates an unique set of powerful stochastic preconditioning algorithms, including both global and local, sequential preconditioners. The role of preconditioning is of key significance for getting fast solutions for both linear and nonlinear stochastic FEA problems. It should be noted that the effects of stochastic preconditioning is larger for nonlinear stochastic FEA problems since it reduces both the number of Krylov iterations for linear solving and the number of Newton iterations for nonlinear solving. The expected speed up coming from stochastic preconditioning is at least 4-5 times for linear FEA problems and about 10-15 times for highly nonlinear FEA problems. The comparative FEA parallel run time results shown in Table 1 show a near ideal speed-up when increasing the number of processors from 6 to18, if the computational size of the problem is large enough to overcome the communication overhead of the parallel FEA.

To compute local stresses in subsystem components, we used traditional response surface models, but also more refined stochastic response surface approximation (SRSA) models. These SRSA models are based on high-order stochastic field models that are capable of handling non-Gaussian variations [4, 5]. The SRSA implementations that are based on two and three level hierarchical density models as shown in Figure 10 for a highly nonlinear response.

Two SRSA models are described herein: i) 3-Level Hierarchical Model (3LHM) and ii) Meshless Fast Probability Integration Model (MPFI).

3-Level Hierarchical Model (3LHM)

The local JPDF models are expanded in two-level of local JPDF models:

$$f(y,\mathbf{x}) = \sum_{i=1}^{n} f(y,\mathbf{x}|s_i)p(s_i,\mathbf{x})$$

$$= \sum_{i=1}^{n} f_i(y,\mathbf{x})p_i = \sum_{i=1}^{n}\sum_{j=1}^{m} f_{i,j}(y,\mathbf{x})\mu_{i,j} \qquad (1)$$

The mixing probability coefficient vector now becomes a mixing partition matrix, whose elements correspond to the conditional probabilities that i will belong to j basis function.

To compute the conditional response PDF we used:

$$f(y|\mathbf{x}) = \frac{f(y,\mathbf{x})}{f(\mathbf{x})} = \frac{\sum_{i=1}^{n}\sum_{j=1}^{m} f_{i,j}(y,\mathbf{x})\mu_{i,j}}{\sum_{i=1}^{n}\sum_{j=1}^{m} f_{i,j}(\mathbf{x})\mu_{i,j}}$$

$$= \frac{\sum_{i=1}^{n}\sum_{j=1}^{m} f_{i,j}(y|\mathbf{x}) f_{i,j}(\mathbf{x})\mu_{i,j}}{\sum_{i=1}^{n}\sum_{j=1}^{m} f_{i,j}(\mathbf{x})\mu_{i,j}}$$

$$= \sum_{i=1}^{n}\sum_{j=1}^{m} f_{i,j}(y|\mathbf{x}) h_{i,j}(\mathbf{x}) \qquad (2)$$

The 2nd order basis functions $h_{i,j}(\mathbf{x})$ can be computed as an expansion in terms of the 2nd order local JPDF models $f_{i,j}(\mathbf{x})$:

$$h_{i,j}(\mathbf{x}) = \frac{f_{i,j}(\mathbf{x})\mu_{i,j}}{\sum_{i=1}^{n}\sum_{j=1}^{m} f(\mathbf{x})\mu_{i,j}} \qquad (3)$$

The conditional-mean surface can be computed by:

$$E[y|\mathbf{x}] = \bar{y}(\mathbf{x}) = \frac{\sum_{i=1}^{n}\sum_{j=1}^{m} E_{i,j}[y|\mathbf{x}] f_{i,j}(\mathbf{x})\mu_{i,j}}{\sum_{i=1}^{n}\sum_{j=1}^{m} f_{i,j}(\mathbf{x})\mu_{i,j}} =$$

$$\sum_{i=1}^{n}\sum_{j=1}^{m} \bar{y}_{i,j} h_{i,j}(\mathbf{x}) \qquad (4)$$

The mixing probability coefficient vector now becomes a mixing probability partition matrix whose elements correspond to the conditional probabilities that i-th data point belongs to the j-th basis function.

The 3LHM models perform extremely well in comparison with other response surface meta-models. The key aspect of the 3L HM implementation is how to optimally define the second-level JPDFs to best approximate stochastic response locally. Figure 11 shows that the 3L HM provides accurate stochastic response approximation for highly nonlinear relationships by using only a reduced number of local JPDF models. The key aspect of the 3L HM implementation is how to optimally define the second-level JPDFs to best approximate stochastic response locally. Figure 11 indicates that 3LHM provides accurate stochastic response approximation for highly nonlinear relationships. Only a reduced number of local JPDF models is required as shown in the left plot (Gaussian clusters).

Stochastic Clustering:

Assuming that local JPDF components are multivariate Gaussians, their analytical expression is given by:

$$f_x(\bar{\mathbf{x}}, \boldsymbol{\Sigma}) = \frac{1}{(2\pi)^{\frac{m}{2}} (\det \boldsymbol{\Sigma})^{\frac{1}{2}}}$$

$$\exp[-\frac{1}{2}(\mathbf{x}-\bar{\mathbf{x}})^T \boldsymbol{\Sigma}^{-1}(\mathbf{x}-\bar{\mathbf{x}})] \qquad (5)$$

where $\bar{\mathbf{x}}$ is the mean vector and a $\boldsymbol{\Sigma}$ is the local component (or cluster) covariance matrix.

For a local component i the covariance matrix is computed by:

$$\sum_i = \frac{\sum_{k=1}^{N} \mu_{i,k}(\mathbf{x}_k - \bar{\mathbf{x}}_j)(\mathbf{x}_k - \bar{\mathbf{x}}_j)^T}{\sum_{k=1}^{N} \mu_{i,k}} \qquad (6)$$

where the factor μ_{ik} that is the conditional probability that data point k belongs to local Gaussian model.

It should be noted that in order to completely define a local Gaussian PDF model i, we need to compute the Mahalanobis distance (the inner product in the above equations), $D(\mathbf{x}, \mathbf{x}_i)$ that is $D(\mathbf{x}, \bar{\mathbf{x}}_i) = (\mathbf{x} - \bar{\mathbf{x}}_i)^T \sum^{-1} (\mathbf{x} - \bar{\mathbf{x}}_i)$ for a Gaussian with an arbitrary orientation.

For arbitrary orientation of the local Gaussian JPDF (clusters), the local covariance is a full matrix, while for parallel orientation is diagonal matrix with the directional variances along diagonal. The principal directions of the covariance matrix define the zero correlation directions. The local Gaussian (cluster) model is elongated along the direction on minimum variance that is defined by the eigenvector of covariance matrix with the smallest eigenvalue.

Fuzzy Clustering:

As an alternate to statistical clustering, we used also fuzzy clustering. As an alternate to the *stochastic* cluster covariance matrix, we also

used the *fuzzy* cluster covariance matrix $\mathbf{F}_i$ defined by

$$\mathbf{F}_i = \frac{\sum_{k=1}^{N} \mu_{i,k}^{m} (\mathbf{x}_k - \bar{\mathbf{x}}_j)(\mathbf{x}_k - \bar{\mathbf{x}}_j)^T}{\sum_{k=1}^{N} \mu_{i,k}^{m}} \quad (7)$$

Usually, the parameter m is equal to 2. The correspondent quantity of the conditional probability is replaced by its fuzzy version that is often called the partition function defined by:

$$\mu_{i,k} = \frac{1}{\sum_{j=1}^{NC} \left(\frac{D(\mathbf{x}_i, \bar{\mathbf{x}}_k)}{D(\mathbf{x}_j, \bar{\mathbf{x}}_k)} \right)^{\frac{1}{m-1}}} \quad (8)$$

In the above equations, the generalized fuzzy distance $D(\mathbf{x}, \mathbf{x}_i)$ has a modified from stochastic version $D(\mathbf{x}_i, \bar{\mathbf{x}}_j) = (\mathbf{x}_i - \bar{\mathbf{x}}_j)^T \mathbf{A}_j (\mathbf{x}_i - \bar{\mathbf{x}}_j)$ where $\mathbf{A}_j = \mathrm{Det}[\mathbf{F}_j]^{1/P} [\mathbf{F}_j]^{-1}$, p is input dimensionality.

These clustering analysis techniques are powerful statistical tools for building soft partitions (clusters) in the sample data space. These techniques have large applications in system control and robot applications.

Meshless Fast Probability Integration (MFPI) Model

The MFPI models are based on two-level hierarchical models. The probability-level response, y_p is computed by solving the one-dimension integral:

$$p = \int_{-\infty}^{y_p} f(y|\mathbf{x})dy = \int_{-\infty}^{y_p} \frac{\sum_{i=1}^{n} f(\mathbf{x}|s_i) f(y|\mathbf{x}, s_i) p(s_i)}{\sum_{i=1}^{n} f(\mathbf{x}|s_i) p(s_i)} dy$$

$$= \int_{-\infty}^{y_p} \sum_{i=1}^{n} f_i(y|\mathbf{x}) h(\mathbf{x}, s_i) dy$$

$$= \int_{-\infty}^{y_p} \sum_{i=1}^{n} f_i(y|\mathbf{x}) h_i(\mathbf{x}) dy \quad (9)$$

The particularity of the MFPI models is than the high-dimensional response surface is never computed on a rectangular grid. If the analyst desires to compute a probability-level response surface or to simulate stochastic response using MFPI models the calculations are done extremely fast using the mixtures of local density models. First, we need to build the JPDF volume of the input-response vector and, then, we need to perform fast integration for to compute the conditional response PDF at each point of interest in stochastic space.

The MFPI surface models can be easily integrated for different probability-levels as desired. Figure 12 shows the application of the 3LHM and MFPI response surface models to the HMMWV LCA stresses at a critical location. The 3LHM response surface is computed for the conditional mean value of the response. The MFPI response surfaces are computed for 50% and 90% probability of non-exceedance. For local density models we used equal-volume fuzzy GK clusters that provide smooth estimated surfaces. It should be noted that for noisy response surfaces the MFPI model behaves better than the 3LHM model as indicated in Figure 12.

PROGRESSIVE DAMAGE MODELS

For fatigue damage modeling, the following models are considered:

Crack Initiation: Stochastic Cumulative Damage Models Using Strain-Life Approach:

1) Linear Damage Rule (Miner's Rule)
2) Damage Curve Approach (NASA Glenn)
3) Double Damage Curve Approach (NASA Glenn)

Crack Propagation: Stochastic Linear Fracture Mechanics-based Models:

1) Modified Forman Model (NASA JPC)

Both the constitutive stress-strain equation and strain-life curve are considered to be uncertain. The two Ramberg-Osgood model parameters and the four strain-life curve (SLC) parameters are modeled as random variables with selected probability distributions, means and covariance deviations.

The strain-life curve including the mean stress effect σ_m on the alternating strain is described by the equation:

$$\varepsilon_a = \frac{\sigma_f'}{E}\left(1-\frac{\sigma_m}{\sigma_f'}\right)(2N_f)^b + \varepsilon_f'(2N_f)^c \qquad (10)$$

We also included correlations between different parameters of SLC. This correlation can significantly affect the predicted fatigue life estimates as shown in case studies section.

We combined rainflow cycle counting with the Neuber's rule for local plasticity modeling for any irregular stress-strain history. For a sequence of cycles with constant alternating stress and mean stress the Damage Curve Approach (DCA) and Double Damage Curve Approach (DDCA) were implemented.

The total damage is computed using a generalized interaction curve between corrosion and fatigue damages:

$$D_{total} = \left[\left(\frac{n}{N}\right)^q + \left(\frac{a_{pit}}{a_{init}}\right)^p\right]^m \qquad (11)$$

Where p, q and m are material parameters that depend on the cumulative damage rules that is applied (please see references for more details).

To compute pit depth two pit growth models were used: i) Power Law and ii) Wei Model. There are described as follows:

Power Law Model:

For a boldly exposed surface, the depth of the deepest pit, a, as a function of exposure time, t, is typically described by a power law,

$$a = At^{1/n} \qquad (12)$$

where A and n are empirically determined parameters with n usually having a value between 2 and 4. The above power law relationship does not mean that any one pit grows at this rate. This equation represents how the maximum of the distribution of pit depth changes with time.

Wei Model:

A spatial pit growth model was proposed by Wei [8]. This pit growth model assumes that the pit shape is a hemispherical shape and its size grows at a constant volumetric rate dV/dt given by

$$\frac{dV}{dt} = 2\pi a^2\frac{da}{dt} = \frac{MI_{p0}}{nF\rho}\exp\left(-\frac{\Delta H}{RT}\right) \qquad (13)$$

By integrating the above equation, the pit depth a at a given time t is given by

$$a = \left\{\left[\frac{3MI_{p0}}{2\pi nF\rho}\exp\left(-\frac{\Delta H}{RT}\right)\right]t + a_0^3\right\}^{1/3} \qquad (14)$$

Where a_0 is the initial pit radius, M is the molecular weight of the material, n is the valence, F=96514 C/mole is Faraday's constant, ρ is density of the material, ΔH is the activation energy, R=8.314 J/mole-K is the universal gas constant, T is the absolute temperature, and I_{P0} is the pitting current coefficient.

In comparison with the linear damage rule (LDR) or Miner's rule, these two damage models predict the crack initiation life much more accurately. The shortcoming of the popular LDR or Miner's rule is its stress-independence, or load sequence independence. LDR is incapable of taking into account the interaction of different load levels, and therefore interaction between different damage mechanisms or failure modes.

There is substantial experimental evidence that shows that LDR is conservative under completely reversed loading condition for low-to-high loading sequences, and severely under conservative for high-to-low loading sequence. For intermittent low-high-low-high-…cyclic loading, the LDR severely underestimates the predicted life. The nonlinear damage models, DCA and DDCA, were implemented to adequately capture the effects of the HCF-LCF interaction and corrosion-fatigue damage for vehicle subsystem components.

Crack propagation was implemented using a stochastic modified Forman model. Both the stress intensity threshold and material toughness are considered as random variables. The stochastic crack growth model considers all the parameters as random quantities, but will include also two additional random factors for modeling uncertainties in the regions of low and high values of the rate da/dN in Regions I and III [9]:

$$\frac{da}{dN} = \frac{C(1-R)^m \Delta K^n (\Delta K - \lambda_{Kth}\Delta K_{th})^p}{[(1-R)\lambda_{Kc}K_C - \Delta K)]^q} \quad (15)$$

The threshold random factor can be adjusted to simulate the uncertain small-crack growth.

Corrosion–fatigue damage effects due to pitting growth were considered by implementing a simultaneous corrosion-fatigue (SCF) model [4]. The total corrosion-fatigue damage in the crack nucleation stage is computed using a generalized interaction curve between corrosion and fatigue damages, while the in crack propagation stage is computed by linear fracture mechanic models (Forman model) for which the stress intensity factors are adjusted based on local crack size including both the fracture crack and the pit depth.

The crack propagation stage is computed by linear fracture mechanics models (Forman model) for which the stress intensity factors are adjusted based on local crack size including both the fracture crack and the pit depth. To include corrosion pit effects the stress intensity range, ΔK, is amplified by a corrosion pitting factor, as follows:

$$\Delta K^{CF} = \Psi(t)\Delta K \quad (16)$$

The pitting factor $\Psi(t)$ depends on both the pit size and the crack size as follows:

$$\psi(t) = \sqrt{1 + \frac{a_{pit}(t)}{a_{crack}(t)}} \quad (17)$$

PROBABILISTIC LIFE AND RELIABILITY PREDICTION

For probablistic life and reliability prediction we considered probabilistic life models based on Lognormal and Weibull probability distributions.

Typically, reliability is quantified by probability of failure (Figure 13). The failure is defined by either reaching the ultimate crack length or reaching the stress intensity crack stability limit. If maintenance effects are considered (Figure 14), then, the reliability metric of interest is the hazard failure rate (HFR) instead of the probability of failure that is defined as the probability of failure per unit time. Average HFR are computed for each maintenance interval between two scheduled maintenance events. A probabilistic mixture model with lognormally distributed components is used for reliability prediction when maintenance is considered.

The instantaneous hazard failure rate at time t is defined as ratio between the time to failure (life) probability density function at time t, f(t), over the reliability function at time t, R(t). Hazard failure rate can be also defined as a function of reliability function or instantaneous risk incremental change:

$$h(t) = \frac{f(t)}{R(t)} = -\frac{1}{R(t)} \cdot \frac{d}{dt} R(t) = \frac{P_f'(t)}{1 - P_f(t)} \quad (18)$$

For a given interval [0, t], the average hazard failure rate can be computed by:

$$h(0,t) = \frac{1}{t} \ln \left| \frac{1 - P_f(0)}{1 - P_f(t)} \right| \quad (19)$$

Other reliability engineering metrics that are popular in practice, such as MTBF (mean time between failures) that are required by many maintenance cost analysis software can be computed by integrating the reliability function (defined by unity minus the failure probability):

$$MTBF = \int_0^\infty [1 - P_f(t)]dt \quad (20)$$

To include the effect of the limited number of stochastic FEA simulation runs on the FLSS reliability we used both parametric and non-parametric bootstrapping techniques.

We also considered the effect of maintenance activities on predicted reliability including uncertainties related to the maintenance schedule, crack detection and sizing (Figure 14), and also the damage repair efficiency. We considered the uncertainties in the maintenance activities that are related to the prediction accuracy of non-destructive inspection (NDI) techniques and component repairs. By developing physics-based stochastic models for idealizing the operating environment, force loading, structural behavior and material progressive corrosion-fatigue damage under variable loading, we approached the maintenance engineering analysis from an advanced physics-based modeling and understanding. Based on physics-based stochastic models, the overall life cycle cost process can be adequately addressed. The actual approaches to risk-based maintenance analysis that are based solely on simple Weibull life models developed for limited tests or field data, that suffer severely from having a weak foundation by neglecting the stochastic physics of failures. An important aspect that affects signficantly aging ground vehicle reliability is corrosion pitting. As shown by many field observations, the effects of pitting can speed up the corrosion-fatigue crack growth by as much as 10 (ten) times.

The critical damage produced by corrosion-fatigue that impacts vehicle reliability is produced by local cracking. The effects of inspections on failure risks were included by specific POD and the crack sizing error curves. To evaluate the NDI techniques, the following probabilities were considered: (1) correctly placing the damage at or above the safety limit, (2) incorrectly placing the damage at or above the safety limit, (3) correctly placing the damage below the safety limit, and (4) incorrectly placing the damage below the safety limit. The second probability contributes to the probability of performing maintenance sooner than necessary. The fourth probability contributes to the risk of unexpected failure.

Available POD and probability of sizing errors for corrosion-fatigue cracking were used in these calculations. When the data for these curves is lacking, the curves were estimated. Sensitivities of the overall joint risk were also determined. In addition, options to add additional POD and probability of sizing error curves for future techniques and situations were implemented. At each inspection, the crack size rejection limit can be specified. If the crack size is greater than the crack size rejection limit, maintenance occurs. Maintenance changes the crack size distribution by removing the identified cracks with sizes above the crack size rejection limit.

BAYESIAN AND NON-BAYESIAN UPDATING

The Bayesian updating procedure includes three basic assumptions:

1) Assume that the PDF of predicted quantity X (called prior PDF) is a function of a set of selected parameters. Thus, $\mathbf{p(x|\theta)}$ is assumed to be known, but the value of the vector $\boldsymbol{\theta}$ is not known exactly. We used a non-analytical form for $\mathbf{p(x|\theta)}$ based on local JPDF models without data clustering
2) Our initial knowledge about $\boldsymbol{\theta}$ is assumed to be contained in a known prior density p ($\boldsymbol{\theta}$). We used the first two statistical moments of $\mathbf{p(x|\theta)}$ as parameters.
3) The rest of knowledge about $\boldsymbol{\theta}$ is contained in the set of data, set D of the n samples $\mathbf{x}_1, \cdots, \mathbf{x}_n$ drawn independently from the unknown p($\mathbf{x}$).

Bayesian updating problem is to compute the posterior density

$$\mathbf{p(x|}\,D) = \int \mathbf{p(x|\theta)p(\theta|D)}\,d\boldsymbol{\theta} \tag{21}$$

where

$$\mathbf{p(\theta|}\,D) = \frac{\mathbf{p(\theta|}\,D)\,\mathbf{p(\theta)}.}{\int \mathbf{p}(D|\boldsymbol{\theta})\mathbf{p}(\boldsymbol{\theta})\,d\boldsymbol{\theta}} = L(D|\boldsymbol{\theta})\mathbf{p}(\boldsymbol{\theta}) \tag{22}$$

and

$$L(D|\Theta) = \prod_{k=1}^{n} p(x_k|\Theta) \quad (23)$$

To solve Bayesian updating, we simulate Θ_i distributed with conditional $p(\Theta|D) = p(\Theta) \cdot L(D|\Theta)$ using MCMC with an energy function equal to the negative loglikelihood – log ($p(\Theta|D)$).

Based on the MCMC simulation, the conditional $p(x|D) = \int p(x|\Theta)p(\Theta|D)d\Theta$ could be estimated by simple statistical averaging. The first-order and second-order statistical moments are computed as follows:

$$E[p(x|D)] = \frac{1}{N}\sum_{i=1}^{N} p(x|\Theta_i) \quad (24)$$

$$Var[p(x|D)] = \frac{1}{N}\sum_{i=1}^{N} [p(x|\Theta_i)]^2 - E[p(x|D)]^2 \quad (25)$$

Where the non-analytical conditional PDF of the quantity x is computed by a probablistic mixture model

$$p(x|\Theta_i) = \sum_{j=1}^{N} \exp\left(\frac{x_j - x(\Theta_i)}{\sigma(\Theta_i)}\right)^2 \quad (26)$$

In addition to the classical Bayesian updating as decribed above that is a "soft" updating procedure based on a "weak form" solution of an integral weighting problem, we also implemented a novel stochastic model updating that couples the Bayesian updating (briefly BU) with a probability transformation (briefly PT) algorithm. The novel stochastic model updating procedure is called Bayesian-Probability Transformation updating, or briefly the BPT updating. The probablity transformation aspect incorporates the stochastic bias function between the statistical predicted data and the experimental data. The novel stochastic model updating combines the "soft" evidence via Bayesian updating with the "hard" evidence via probability transformation. The improvement is exceptional as it is shown in the case studies section.

MODELING UNCERTAINTIES

The key categories of modeling uncertainties that are associated with stochastic modeling for computational reliability analyses are due to: (i) lack of sufficient collection of data (small sample size issue), (ii) non-representative collection of statistical data with respect to the entire statistical population characteristics or stochastic system physical behavior (non-representative data issue), (iii) lack of fitting of the stochastic model with respect to a given statistical dataset, i.e. a bias is typically introduced due to smoothing (model statistical-fitting issue) and (iv) lack of accuracy of the deterministic prediction model with respect to real system physical behavior for given input data points, i.e. a bias is introduced at each predicted data point due to prediction inaccuracy (model lack-of-accuracy issue). It should be noted that the first two categories of modeling uncertainty are associated with uncertainties in statistical data collection, while the last two categories are related to modeling uncertainties in prediction models due to statistical smoothing and prediction error.

For incorporating modeling uncertainties in our risk predictions, we need to build a stochastic model space assuming that the statistics of stochastic models are random variables. By randomizing the statistics (called also hyper parameters) of a given stochastic model we define a parametric stochastic model or equivalently a family of stochastic models or a stochastic model space. Since the risk predictions are conditioned on a given stochastic model, the model space and simulated data space are two nested spaces. The outer loop is over the stochastic discrete model space (stochastic model space) and the inner loop is over the stochastic input parameter space (stochastic data space).

A two-level nested simulation loop was implemented for including the effects of a limited number of statistical FEA simulations on predicted risks. It should be noted that the two-nested simulation loop approach requires a number of computational FE analysis runs that is equal to the product of the simulation numbers of the inner loop (stochasticity effects) and outer loop (modeling uncertainty effects). To make numerically efficient the application of the two-nested loop approach we implemented non-

parametric bootstrapping techniques that can be applied either at the local stress level (intermediate level) to avoid performing a large number of FE analyses or at the life prediction level (end level).

SENSITIVITY STUDY RESULTS

In this section we present selected results of a series of sensitivity studies. The output variables are considered the vehicle dynamic response and the local stresses at critical locations, predicted lives and reliability of FLSS for different stochastic input scenarios. We also address the modeling uncertainty effects, stochastic model updating and the maintenance uncertainty effects.

Firstly, we focus on the effect of the stochastic road profile non-Gaussianity. Figure 15 shows the FLSS responses for a Gaussian and a non-Gaussian straight, moderate roughness road profiles for a vehicle speed of 30 mph. The Gaussian and non-Gaussian road profiles have the same second-order statistical moments or power spectral densities. It should be noted that the local stress cycles at a critical location in LCA have about twice larger maximum amplitudes for non-Gaussian profile than for Gaussian profile. For different critical locations within FLSS, the predicted life is about 4 to 40 times shorter for non-Gaussian profile than for Gaussian profile. These results infirm the current practice that is based on the use of Gaussian process models for road profile idealization.

Next, we considered the effect of the road profile topography on the FLSS stress and life. We considered three types of simulated road profiles: i) straight profile (S) with a bump, ii) horizontally curved profile (long turns, LT) and iii) sloped and curved profile (rolling hills, RH). Figure 16 shows the effect of topography for a moderate roughness road profile on the FLSS joint forces. It should be noted that the effect of topography is important. The FLSS joint forces have several times larger amplitudes if topography effects are included.

Figures 17 and 18 show the FLSS LCA ball joint lateral force variation and, respectively, the local Von-Mises stress variations (history and stress range) and the associated rainflow matrix (in alternating strain and mean stress coordinates) at a critical location in the FLSS LCA system.

It should be noted that the maximum stress variation at the selected critical location is about ten times larger for the road profile with topography variation than for the straight road profile, although the road surface roughess is high for the simulated segment considered. For the S profile the maximum stress range amplitude is about 0.50 units if the bump is excluded, while for the RH profile the maximum stress range amplitude is about 5.30 units, and for the LT profile is 3.60 units.

Next, we show the predicted life sensitivity due to slight changes in the nonlinear statistical correlation between the strain-life model random parameters. Please note that the marginal probability distributions of the strain-life model parameters are maintained the same. Changes are only in the correlation structure between these random parameters. Herein, we consider the crack initiation life based on stochastic strain-life curve models. There are four stochastic parameters, σ_f, ε_f, b and c (equation 10) that are included in the probablistic strain-life model.

To include the nonlinear correlation between different stochastic input parameters, we used a generalized marginal probability transformation (GMPT) approach to represent the non-Gaussian joint probability density of those variables by their Gaussian images (also called translational fields) applied in conjuction with statistical clustering for computing mixture-based joint PDFs. We believe that this GMPT approach is accurate, robust and efficient.

Figures 19 and 20 show the effect on nonlinear correlation between the 4 parameters of the strain-life curve for two case studies. Figure 19 shows the data points for the nonlinearly correlated parameters paired as X1(b) and X2 (σ_f) and X3 (c) and X4 (ε_f) for two statistical

databases, Database A (higher correlation) and Database B (lower correlation).

Figure 20 compares the simulated strain-life curve obtained for the statistical Database A (higher correlation) and Database B (lower correlation). It should be noted that the resulting scatter of the two simulated strain-life curve is very different. As an example, if we consider the lowest strain-life curve sample for a given strain range of 2.0E-3, then, the computed fatigue cycle life is only 100 cycles for Database B, but 50,000 cycles for Database A. This drastic change in the computed fatigue life is a solely result of changing the correlation patterns between the strain-life curve parameters (Figure 19). It should be noted that the marginal statistical moments and PDFs were preserved. The correlation pattern change was this only change that was made between Database A and Database B (the marginal PDFs are not modified at all).

It is obvious that this very simple example shows how important is for an accurate life prediction to capture correctly the complex statistical dependences, i.e. nonlinear statistical correlation patterns, between the strain-life curve parameters. Same remarks could be extended to crack propagation models such as Paris Law or Forman linear-fracture mechanics-based models. *This is an extremely important probabilistic modeling aspect that is most often ignored in practical applications.* We hope that these results presented here in this paper will alert and will bring more awareness on this delicate modeling aspect to the non-deterministic engineering community.

Figure 21 shows the effect the progressive damage modeling on the FLSS life prediction. The linear damage rule (LDR) provides a life that is twice as long as the predicted life using a nonlinear damage rule such the damage curve approach (DCA). These results show that the unconditional use of LDR for any fatigue damage modeling could produce crude reliability analysis results. It should be noted that the two progressive damage models LDR and DCA for crack nucleation were combined with the stochastic Forman model for crack propagation [4].

Figure 22 illustrates the effect of lack of data, for 280 stochastic FEA simulations, on the probabilistic life prediction at a critical location of the FLSS LCA system. Both Weibull and lognormal life probabilistic models were considered. It should be noted that Weibull life model provides much shorter predicted lives for a given reliability level. For 99% reliability level, the mean Weibull life is 300 units in comparison with the mean lognormal life that is 750 units. The significant conservatism of the Weibull probablistic model is a main reason of the popularity of these models in engineering practice.

Table 2 shows also the effect of modeling uncertainty on the FLSS predicted life due to the limited number of FEA simulations, only 250 samples, for different selected reliability levels, including mean, 99% and 95% exceedance probabilities. It should be noted that the 99% reliability life is about half of the 95% reliability life. Also the 99% reliability life is about 15-20 times shorter than the mean life. The effect of modeling uncertainty for the 95% confidence versus the 50% confidence is to reduce the 95% and 99% reliability lives by about 20-30%. Figure 23 shows graphically the results presented in Table 2.

Further, we investigated the application of the Bayesian updating for computing the updated bivariate fatigue stress probability distribution based on available experimental data. The bivariate fatigue stress distribution includes both the quasi-static stress component (in X direction in the plots) and the vibratory stress component (in Y direction in the plots).

We considered 5 random test data. The 5 experimental test data were considered by randomly selecting 5 predicted data. This imply that the test data and simulated data are identical, or in other words that the prediction accuracy is perfect. The original and updated PDF of the bivariate stress using Bayesian updating (BU) is shown in the Figure 24 left plot. It should be

noted that the updated PDF departs from original PDF even the prediction accuracy is perfect. Next we consider 25 random test data in the same way. Thus, the prediction accuracy was again perfect. The Bayesian updating result is still poor as shown in the Figure 25 left plot. Comparatively we used the BPT updating that incorporates the test data bias information. The results are shown in the right plots of the two investigated cases with 5 and 25 random test data. As expected, BPT provides an updated PDF that overlapps practically with original PDF since prediction accuracy is perfect.

The above results show a very serious pitfall of the classical Bayesian updating that is currently extremely popular and widely applied by engineers as a black box. This paper pulls a serious alarm for the Bayesian updating application to typical engineering reliability problems.

Figures 26 through 29 show results of selected FLSS sensitivity studies that investigated the effects of i) road surface roughness, ii) road topography, iii) corrosion pitting, and iv) FE modeling uncertainty of local stresses. Each of these effects is signficant. However, road surface roughness and topography have much larger influence of predicted life than corrosion and local stress uncertainty (assuming a 15% c.o.v.).

Finally, we discuss the effects of maintenance uncertainties on the FLSS reliability. The maintenance sensitivity study results are shown in Figures 30 through 33. First, we investigated the case of when the target reliability level or POF is given and the schedule of maintenance events needs to be determined. Results are presented in Table 3 and Figure 30. Three cases were considered for the POF equals to 1.0E-05, 1.0E-04 and 1.0E-03.

Using the developed integrated reliability framework, we determined the required maintenance schedule, the number of scheduled maintence events (SME), the maintenance intervals, the cumulative number of repairs, the instantaneous failure probabilities (POF) and the mean hazard failure rates (MHFR) per maintenance intervals. It should be noted that for the 1.0 E-05 target POF, the numbers of scheduled maintenance events and the number of repairs are both about twice than the number of maintenace events and the number of repairs needed for the 1.0 E-03 target POF. This indicates a scheduled maintenance cost of 4 times higher for the 1.0 E-05 POF than the 1.0 E-03 POF. However, the real risks are shown by the MHFR results not instantaneus POF. The MHFR show a risk ratio over time that is about 50 times larger for the 1.0 E-03 target POF case.

It should be noted that the maintenance intervals are in days that include 24 hours of continuous driving of the HMMWV on moderate roughness profiles. If we assume that HMMWV is driven only 10 hours per day on rough roads, then, the maintenance intervals in real time are much longer as shown in the 4th column of Table 3.

We also studied the effects of the maintenance interval, inspection technique, inspection operator skills and crack size rejection limit criterion on the FLSS reliability as shown in Table 4. The largest impact on reliability is produced by the maintenance scheduling and the inspection operator skills. An unskilled operator could increase the fatigue failure risks by tens of times comparing with a highly skilled operator. Training and environment control are key factors to ensure skilled operators.

The effect of the selected inspection technique on the FLSS reliability is important. We considered Eddy Current inspection versus Visual inspection for cracking detection. All maintenace intervals are 185 days, each day including 24 hour driving on moderate roughness roads. Results show that the Eddy Current inspection is 6-7 times safer than Visual inspection at twice cost (based on the cumulative number of repairs).

Figures 31, 32 and 33 show the effects of inspection technique, operator skills and crack size rejection limit on the computed POF and MHFR. The plotted results are the same with those included in Table 4.

CONCLUSIONS

An integrated HPC reliability framework has been developed to address the many challenges of the ground vehicle reliability prediction problem. The integrated reliability framework includes innovative computational tools that provided a great efficiency to the overall HPC implementation. These innovative tools include advanced stochastic models for road profiles, stochastic FE techniques including stochastic domain decomposition and stochastic preconditioning, three-level hierarchical (3LHM) and meshless fast probability integration (MFPI) models for stochastic response approximation, stochastic progressive damage models for fatigue and corrison fatigue. Both Bayesian and non-Bayesian updating schemes are applied for aggregating the information from predicted data and test data. An efficient two-nested loop simulation algorithm is implemented for incorporating modeling uncertainty effects due to lack of data using bootstrapping or MC simulation. Including modeling uncertainties, variation bounds (confidence intervals) of the predicted risks are determined.

The integrated vehicle fatigue reliability prediction approach incorporates the following steps:

i) simulation of the stochastic operational environment,
ii) stochastic vehicle multi-body dynamics analysis,
iii) stress prediction in subsystems and components,
iv) stochastic progressive damage analysis, and
v) component life prediction, including off-line maintenance and on-line monitoring
vi) reliability prediction at vehicle subsystem level.

The integrated HPC reliability framework is demonstratively applied to the HMMWV front suspension system. The paper shows that the road surface roughness and the road topography variations impact severely on the HMMWV suspension system reliability. The road surface variations are highly non-Gaussian, being rightly-skewed toward larger amplitudes. The non-Gaussian variation aspects of the road profiles have a significant impact on the predicted vehicle fatigue reliability. This is a very important modeling aspect that was ignored in practice over a long period of time. The paper also shows that including the appropriate statistical nonlinear correlation between the stochastic life model parameters, and the effect of the limited number of FEA simulations impacts significantly on the HMMWV suspension reliability prediction.

A variety of sensitivity studies are shown to highlight qualitative aspects of the HMMWV reliability analysis and indicate the governing life parameters for the front suspension reliability, including also the uncertainties in maintenace activities.

ACKNOWLEDGEMENTS

The authors would like to thank to Justin Madsen, graduate student at University of Wisconsin at Madison, who performed a large number of HMMWV simulations. We also acknowledge the DOD SBIR funding support for GP Technologies, Inc. and University of Wisconsin at Madison under the DOD SBIR A06-224 topic DOD contract.

REFERENCES

[1] Gipser, M. "FTire: a physically based application-oriented tyre model for use with detailed MBS and finite-element suspension models." Vehicle Systems Dynamics 43 Supplement: 76 - 91, 2005
[2] Aardema, J. “Failure analysis of the lower rear ball joint on the High-Mobility Multipurpose Wheeled Vehicle.” U.S. Army Tank-Automotive Command Technical Report # 13337, Warren, MI, 1988
[3] Ghiocel, D.M., Lamb, D. and Hudas, G.,”Advances in Computational Stochastic Mechanics and Reliability Prediction for Ground Vehicles”, 2007 SIAM Conference “Mathematics for Industry”, October 2007

[4] Ghiocel, D.M. and Tuegel, E., "Reliability Assessment of Aircraft Structure Joints Under Corrosion-Fatigue Damage", *Engineering Design Reliability Applications: For the Aerospace, Automotive and Ship Industries*", eds. Nikolaidis, Ghiocel and Singhal, CRC Press, September 2007

[5] Ghiocel, D. M. "Advances in Computational Risk Predictions for Complex, Large Size Structural Engineering Applications" *46th AIAA/ASME/ASCE/AHS/ASC Structures, Structural Dynamics & Material Conference*, AIAA-2005-2222, Austin, TX, April 18-21, 2005

[6] Ghiocel, D.M.,"Stochastic Simulation Methods for Engineering Predictions", *Chapter 20 in "Engineering Design Reliability Handbook"*, eds. Nikolaidis, Ghiocel and Singhal, CRC Press, December, 2004

[7] Madsen, J, Ghiocel, D.M., Lamb, D., Gorsich, D. and Negrut, D., "A Stochastic Approach to Integrated Vehicle Reliability Prediction", Proceedings of the ASME 2009 International Design Engineering Technical Conferences & 7th International Conference on Multibody Systems, Nonlinear Dynamics, and Control, IDETC/MSNDC, 2009

[8] Harlow, D.G. and Wei, R.P. "Probability Approach for Prediction of Corrosion and Corrosion Fatigue Life", AIAA Journal, Vol.32, No. 10, 1994, p2073-2079

[9] Moore, N., Ebbeler, D. H., Newlin, L.E., Surtharshana, S., and Creager, M., "An Improved Approach for Flight Readiness Certification – Probabilistic Models for Flaw Propagation and Turbine Blade Fatigue Failure, Volume 1", NASA-CR-194496, Dec. 1992.

Table 1: Scalabillity Study Run Time Results (sec.) for 3D Elastic Problem with Variable Sizes From 100K to 20M DOFs Using From 6 to 24 Processors

Block Jacobi

Num Procs / Equations	100 k	500 k	1 M	5 M	10 M	20 M
6	2.68	14.81	31.24	196.32	443.74	1084.97
12	3.84	10.9	21.66	118.51	260.54	661.36
18	3.61	10.14	19.99	99.99	207.76	508.6
24	4.91	10.42	21.14	92.37	187.42	450.98

Parallel Algebraic Multigrid

Num Procs / Equations	100 k	500 k	1 M	5 M	10 M	20 M
6	3.31	18.53	36.7	174.71	339.25	686.57
12	3.88	11.95	21.51	95.87	178.3	373.51
18	4.5	11.44	17.74	69.49	126.8	259.5
24	6.01	9.55	18.58	57.26	100.68	205.7

Table 2. Modeling Uncertainty Effects on FLSS Probablistic Life for Different Reliability Levels Using Lognormal PDF Model

Road Profile Type (including topography)	Mean Life (days)	Life with Given Reliability 99% and 95% (days)	No Modeling Uncertainty	With Modeling Uncertainty	
			Deterministic	50% Confidence	95% Confidence
High Roughness	620	99%	31	30.0	25.5
		95%	72	72.5	63.9
Moderate Roughness	3200	99%	249	235.8	180.7
		95%	459	462.1	373.8

Table 3. Required Maintenance for FLSS for Different Target Failure Probability (POF) Levels for Moderate Roughness Roads Including Topography Effects with Operating Speeds up to 30 mph (No Additional Armour Weight Included)

Target Probability of Failure (POF)	Computed Probability of Failure (POF)	Number of Scheduled Maintenance Events	Mean Maintenance Interval (days)	Cumulative Number of Repairs per Component	Mean Hazard Failure Rate For Entire Period (per day)
1.0 E-05	1.1 E-05	23	155 (372) (1.02 years)	18	7.5 E-08
1.0 E-04	1.1 E-04	17	205 (492) (1.35 years)	15	5.3 E-07
1.0 E-03	1.0 E-03	12	285 (684) (1.87 years)	11	3.5 E-06

Table 4. Maintenance Analysis Sensitivity Studies for FLSS Reliability for Moderate Roughness Roads Including Topography Effects with Operating Speeds up to 30 mph (No Additional Armour Weight Included)

Sensitive Study Parameters	Average Maximum POF Per Interval	Average Hazard failure Rate	Number of Repairs Per 100 Parts
Maint. Interval=155 days	1.29003e-5	8.32275e-8	853
Maint. Interval=185 days	5.39682e-5	2.91720e-7	745
Maint. Interval=230 days	2.56768e-4	1.11638e-6	617
Visual Inspection *	3.4119e-4	1.84428e-6	382
Eddy Inspection *	5.39682e-5	2.91720e-7	745
Worst Skill Operator *	2.37889e-3	1.28589e-5	280
Best Skill Operator *	3.38781e-5	1.83125e-7	384
Rejection crack size = 0.0 in*	5.39682e-5	2.91720e-7	745
Rejection crack size = 0.15 in*	1.79505e-4	9.70295e-7	170

NOTE: * Constant maintenance intervals of 185 days were considered.

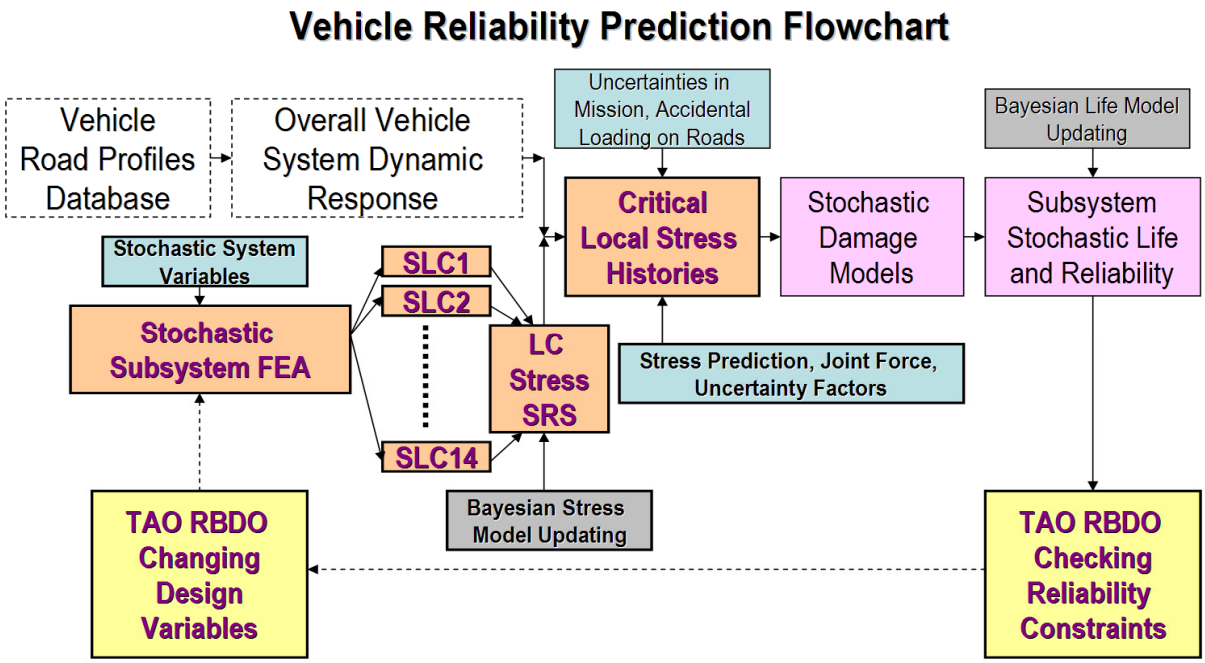

Figure 1 Vehicle reliability prediction flowchart [3]

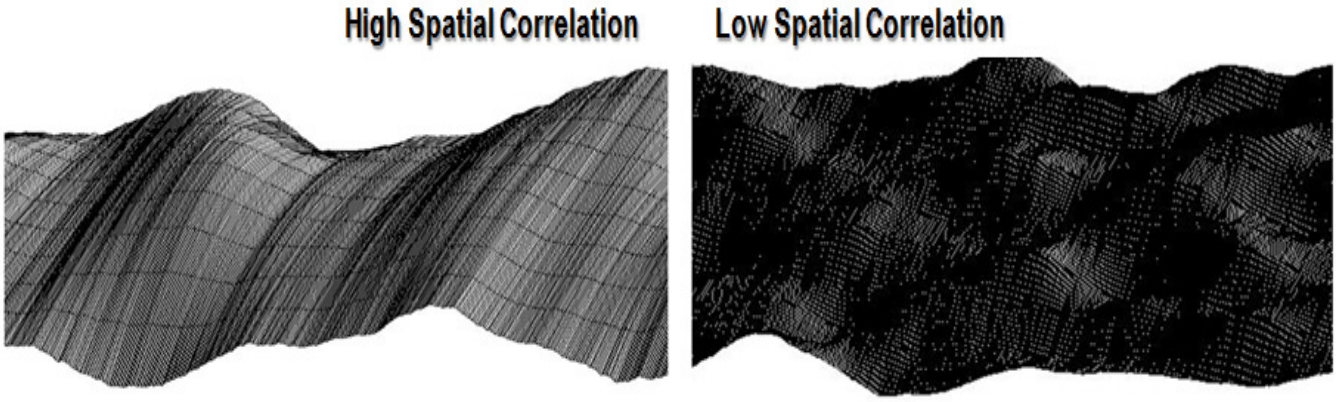

Figure 2 Simulated road surfaces with high (left) and low (right) transverse spatial correlations

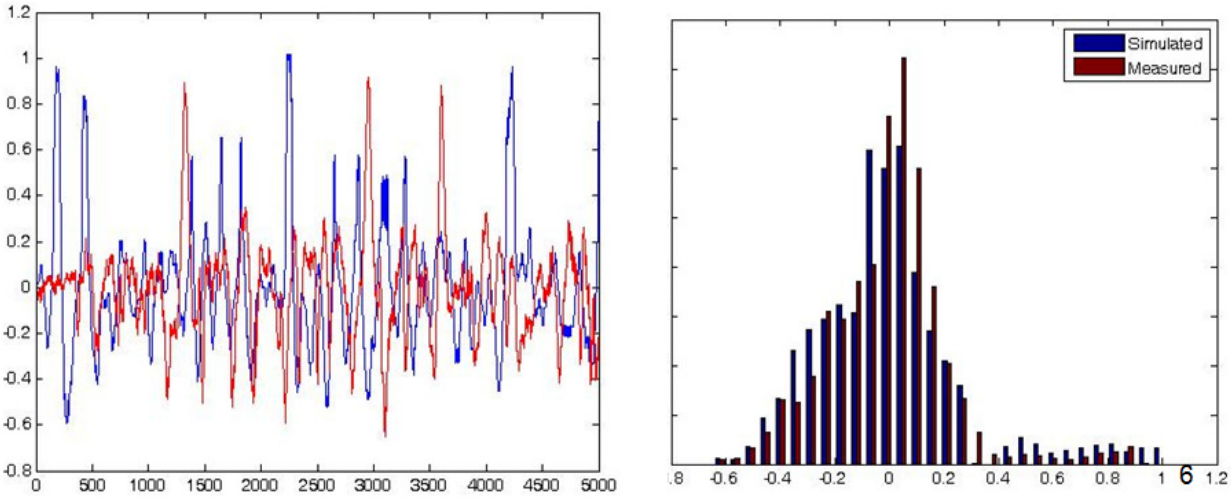

Figure 3 Simulated (blue) and measured (red) road profiles (left plot) and their PDF (right plot)

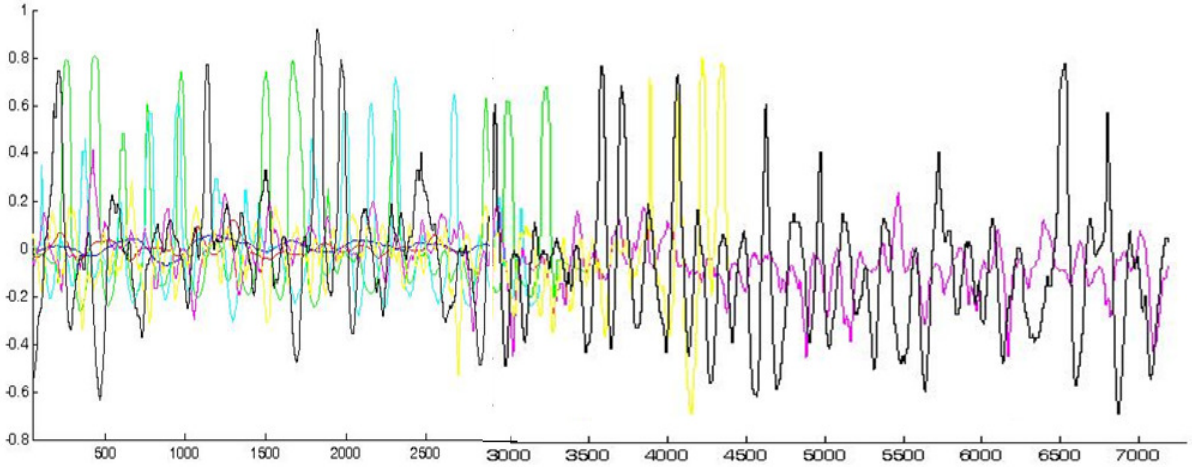

Figure 4 Simulated road profiles (stationary segments) for different road roughnesses

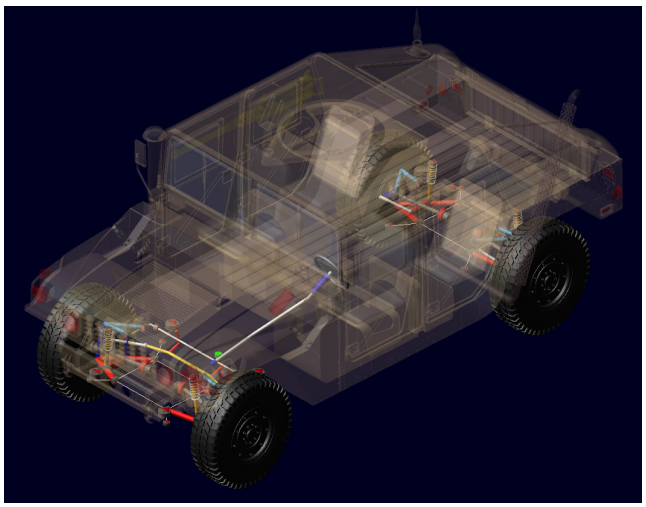

Figure 5 HMMWV Dynamic Model

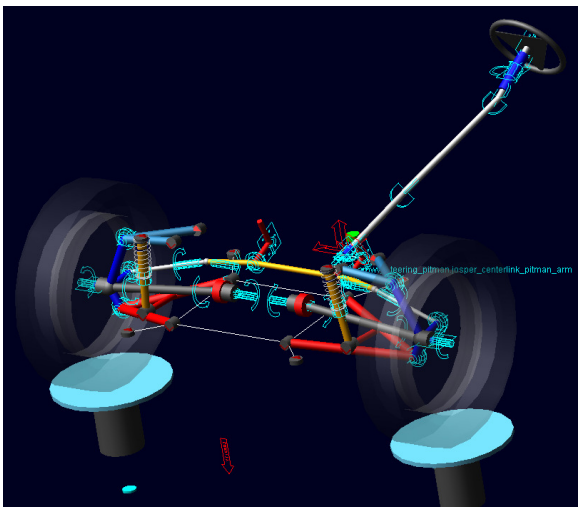

Figure 6 Front Suspension System Model

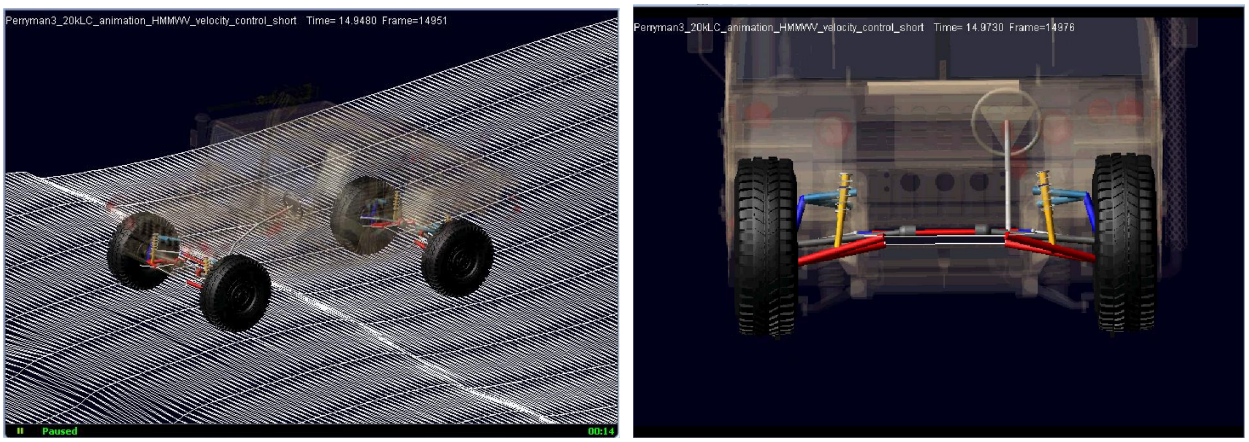

a) Flat road with no topography Effects; Passing a Random Bump

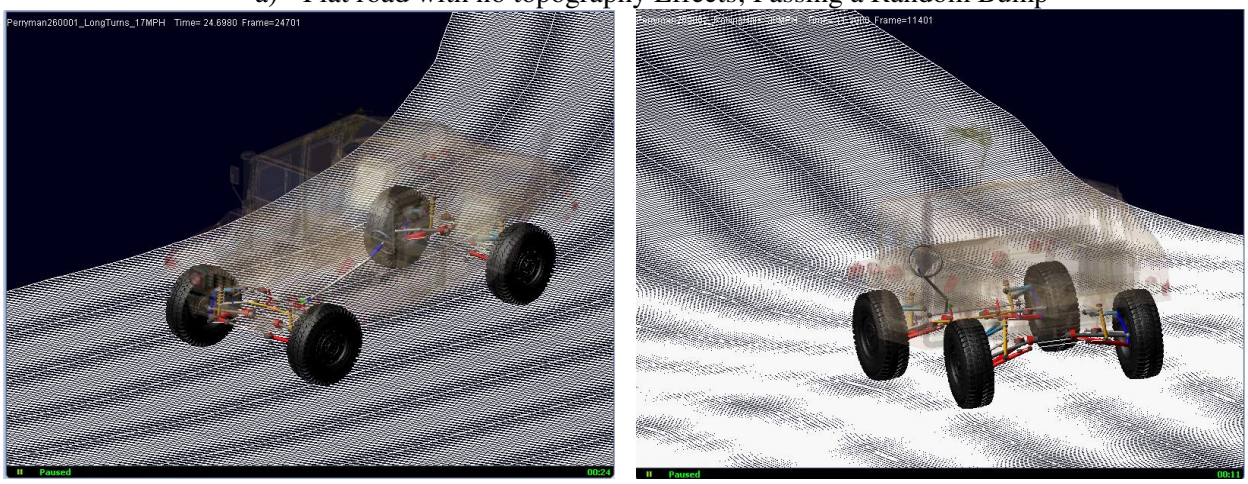

b) With topography Effects; Smooth and Rough Stochastic Roads

Figure 7 HMMWV Simulations with Stochastic Road Profiles

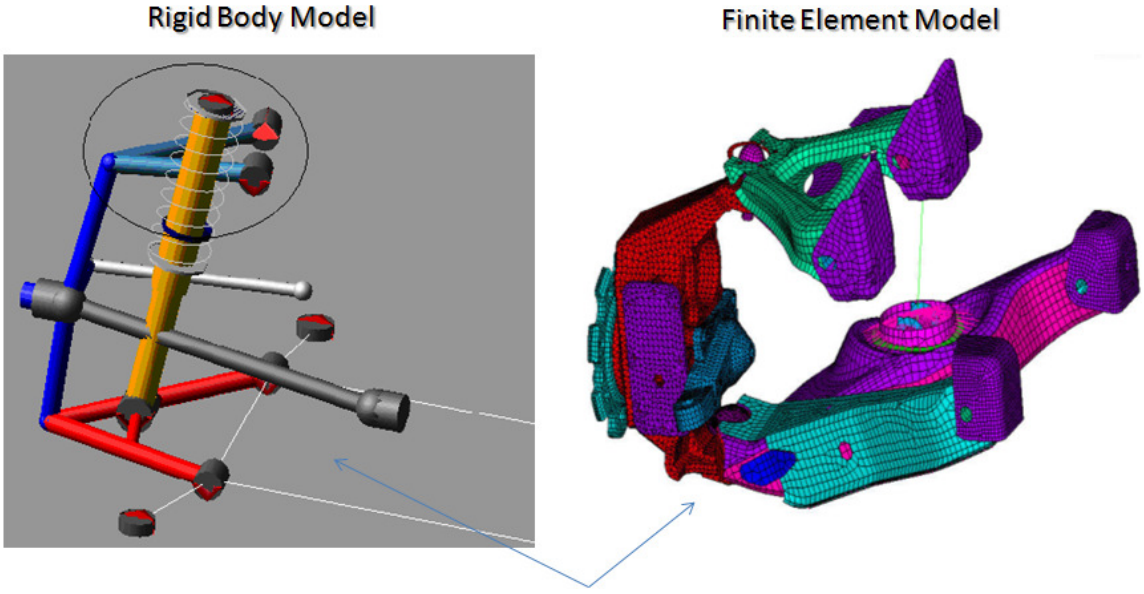

Figure 8: Front-Left Suspension System (FLSS); Vehicle model (left), and FEA model (right)

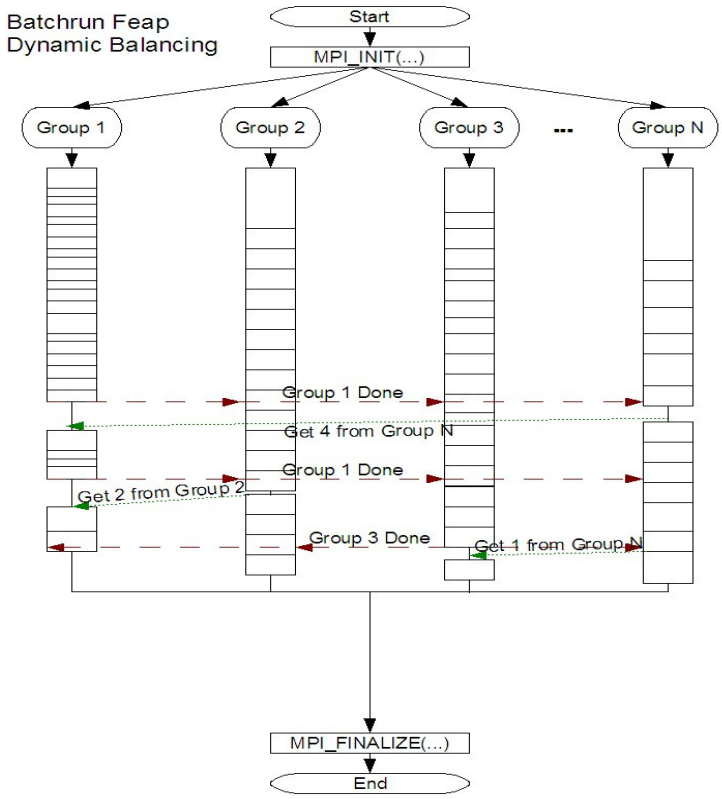

Figure 9 HPC CDD Implementation

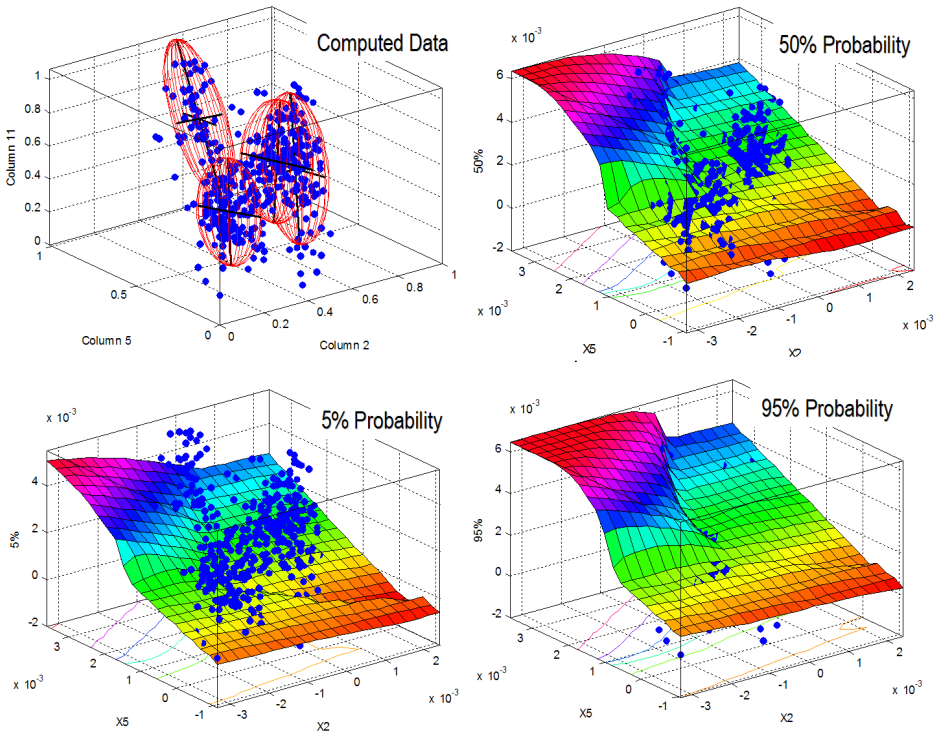

Figure 10 Stochastic Response Surface Approximation (SRSA) Model

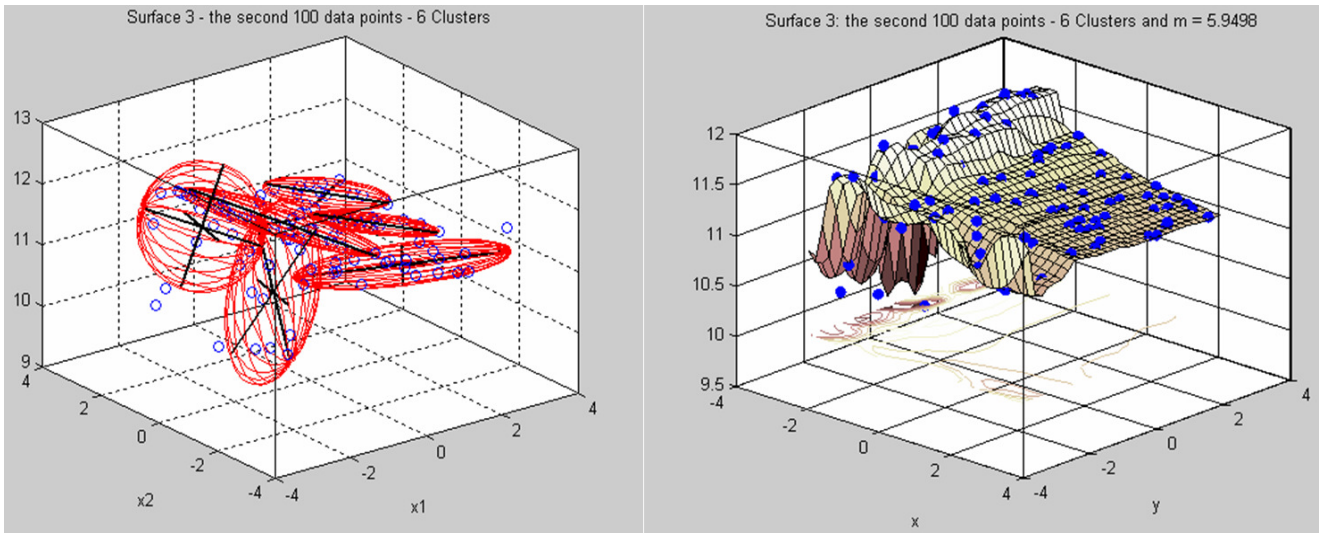

Figure 11 Stochastic Highly Nonlinear Response Surface Approximation Using 3L HM; local JPDF models (left) and conditional mean response surface (right)

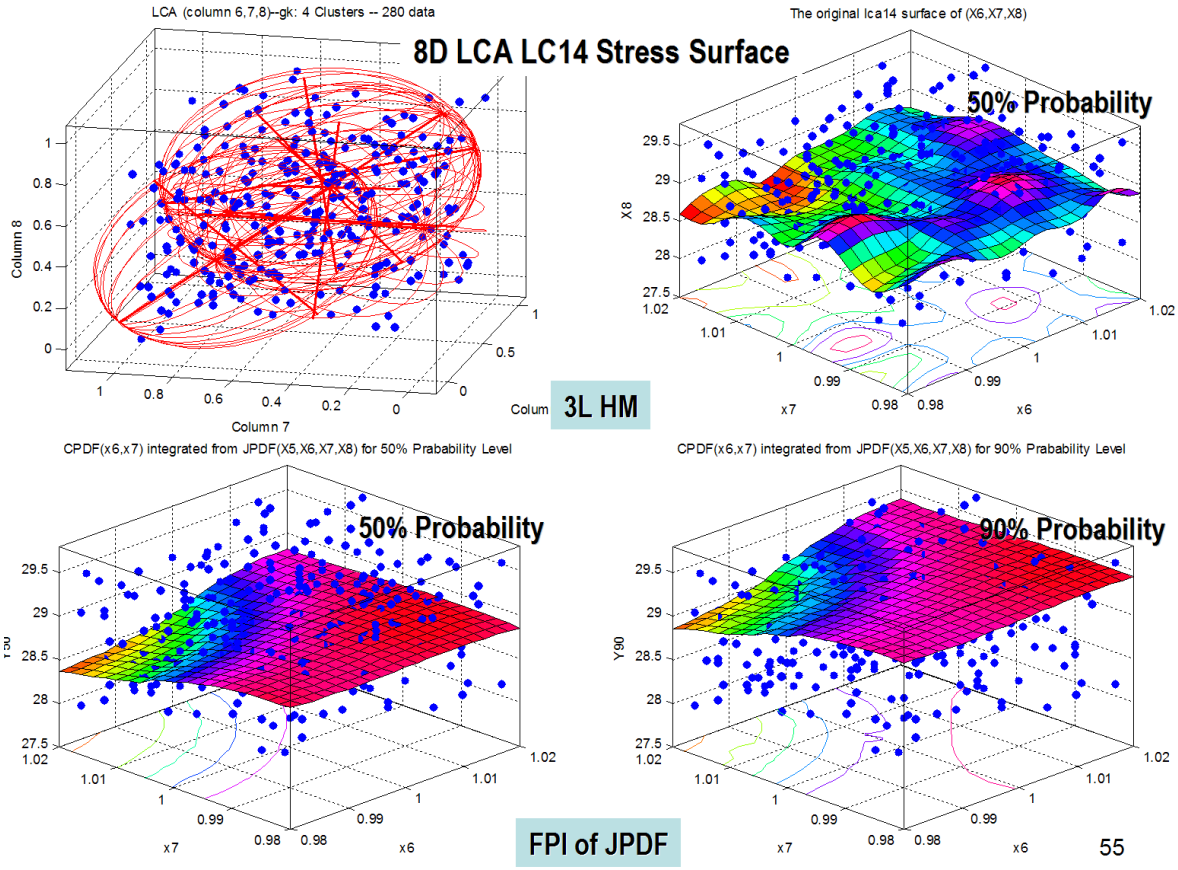

Figure 12 3LHM and MFPI Response Approximation Models for the HMMWV LCA LC#14 Stress

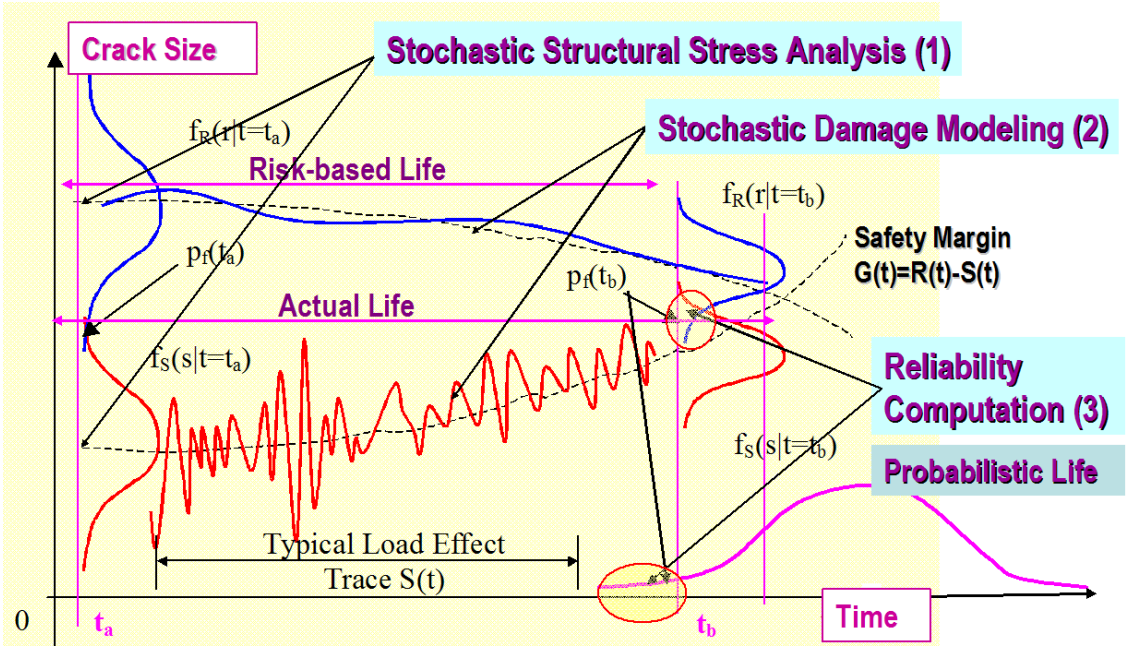

Figure 13 Time-Variant Reliability Analysis Metrics

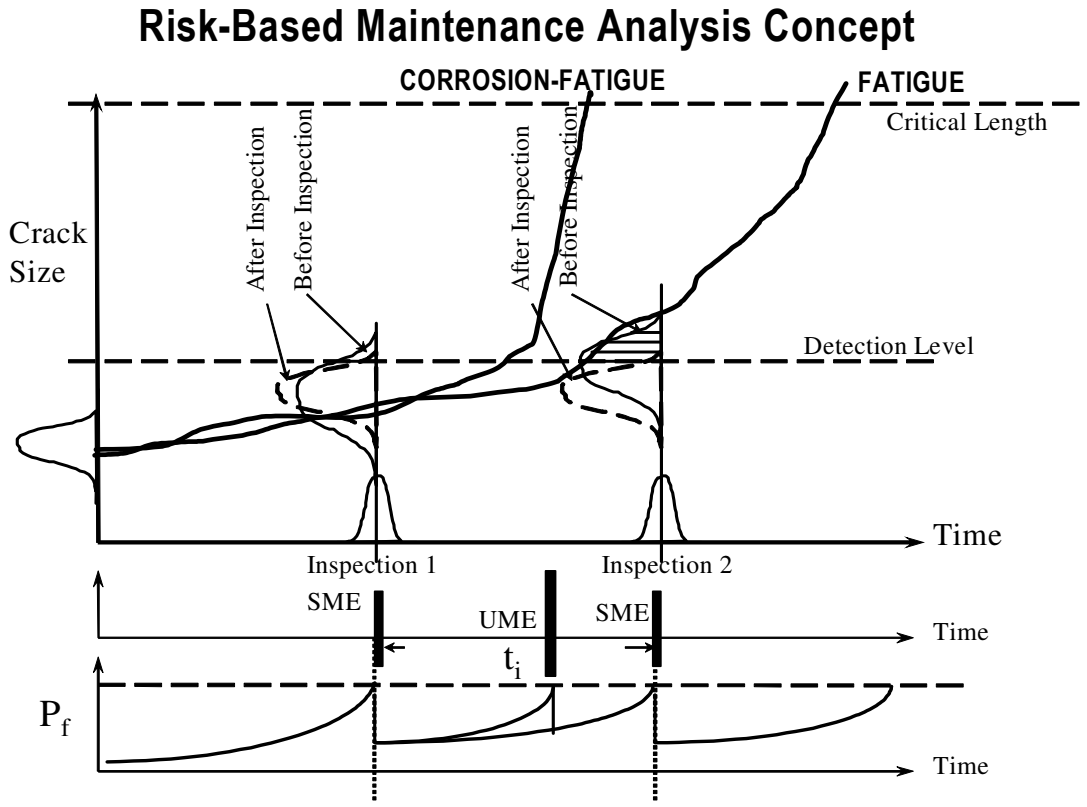

Figure 14 Reliability Prediction Including Uncertainty Effects of Maintenance Activities

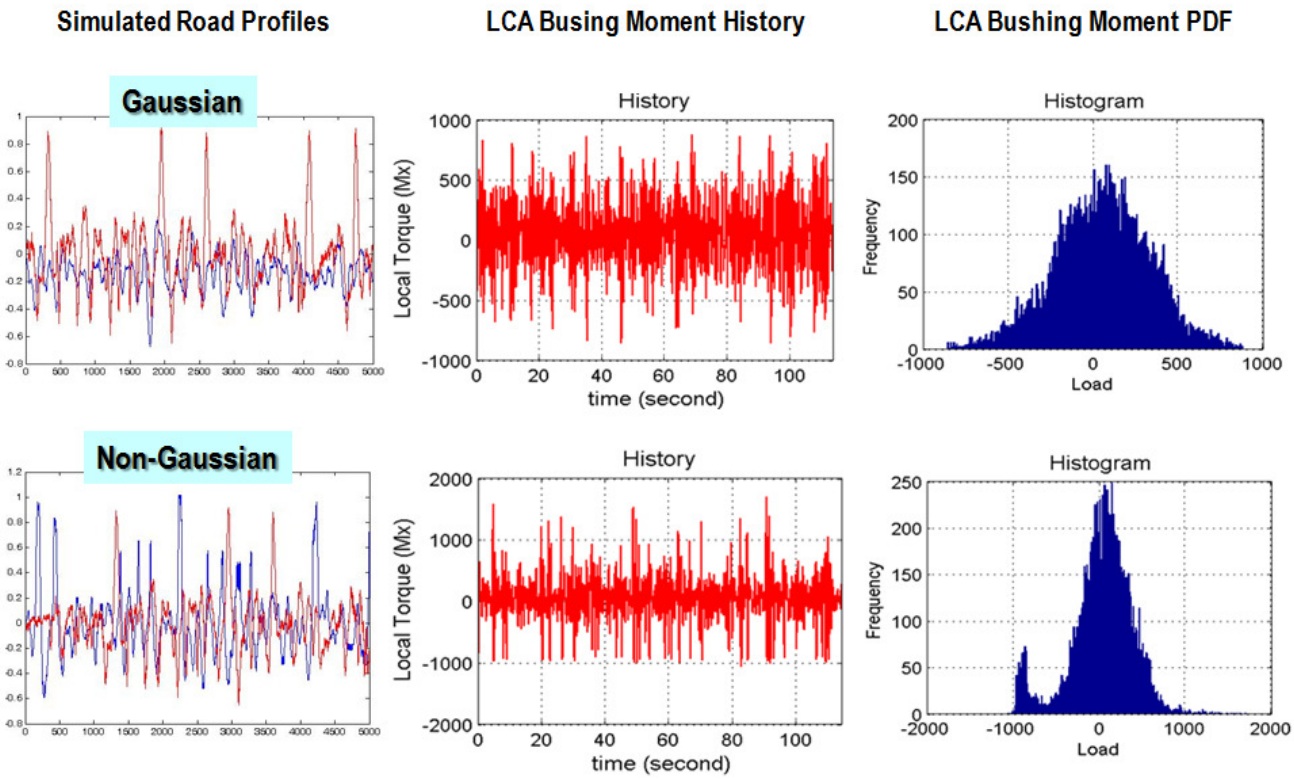

a) Measured and Simulated Road Profiles, Gaussian and Non-Gaussian, and Associated LCA Bushing Torque Moment Histories and PDF Estimates

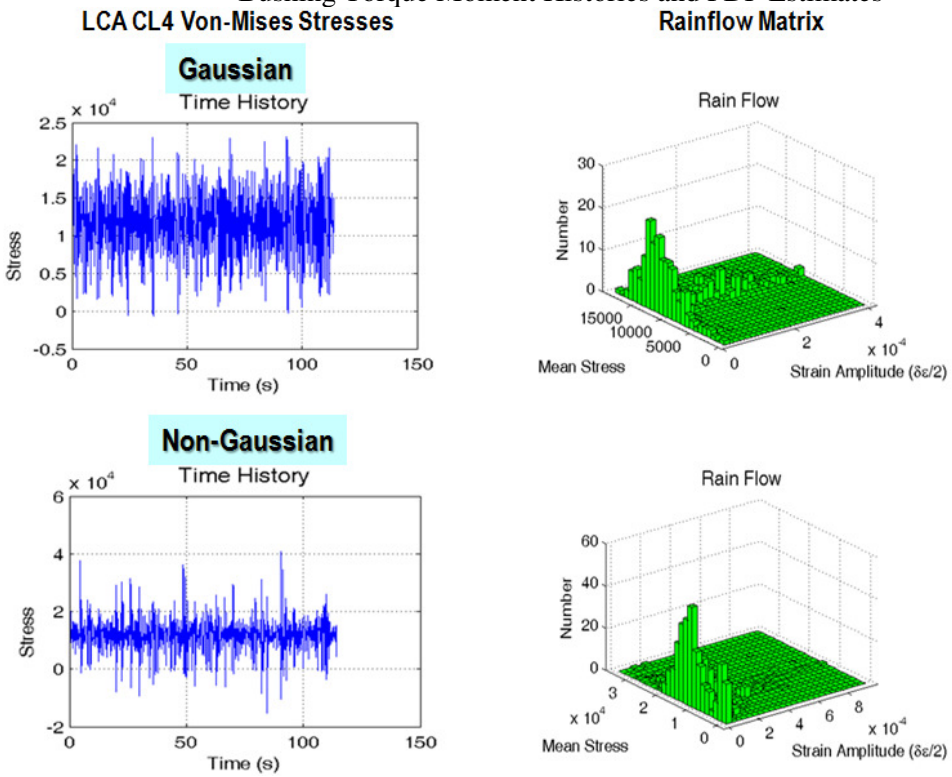

b) Simulated Local Stress Histories and Rainflow Matrices at A Critical Location in LCA

Figure 15 Vehicle FLSS Response for Gaussian and Non-Gaussian Road Profiles at 30 mph

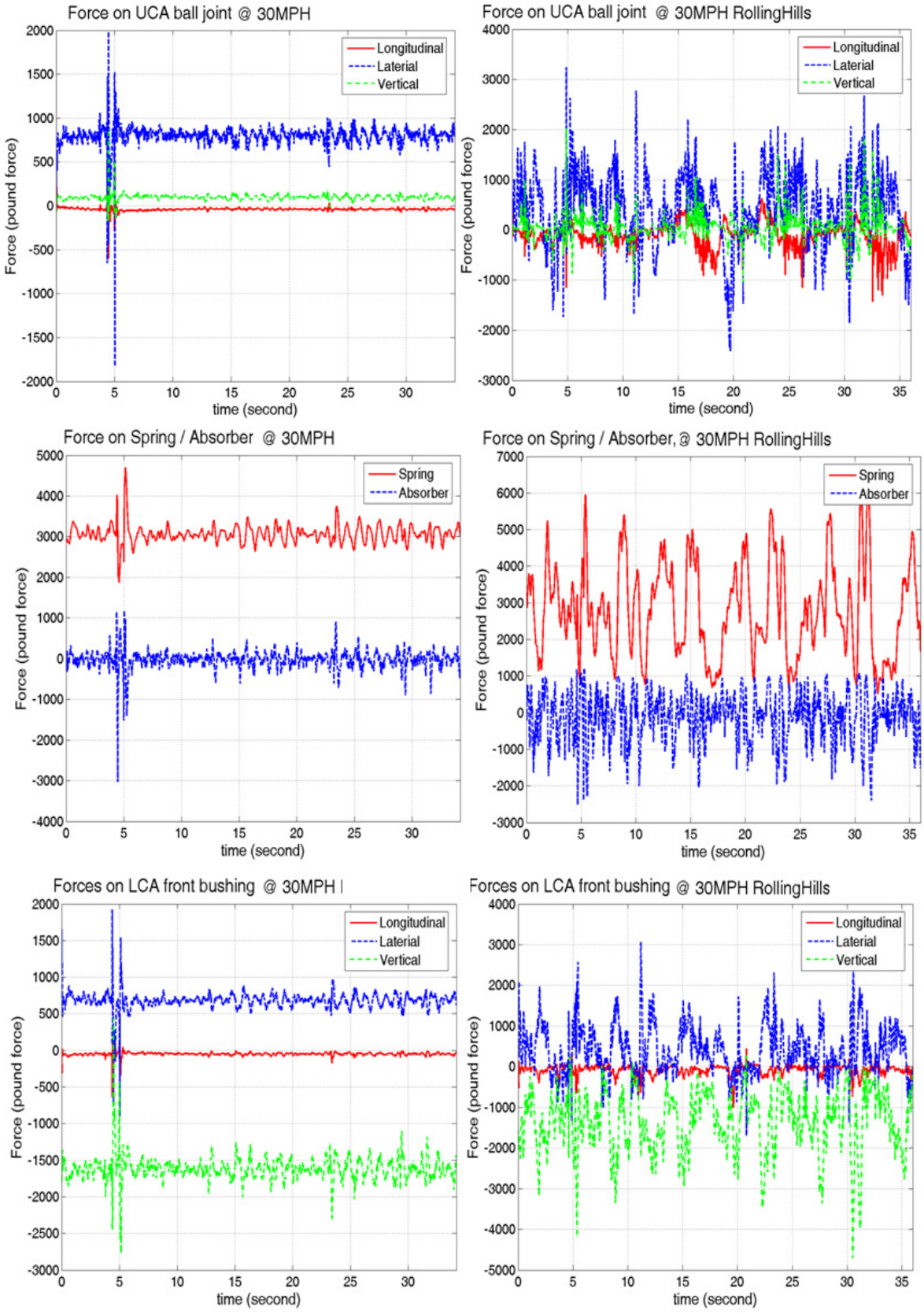

Figure 16 Joint Force Histories for S Profile (no topography) and RH Profile (with topography)

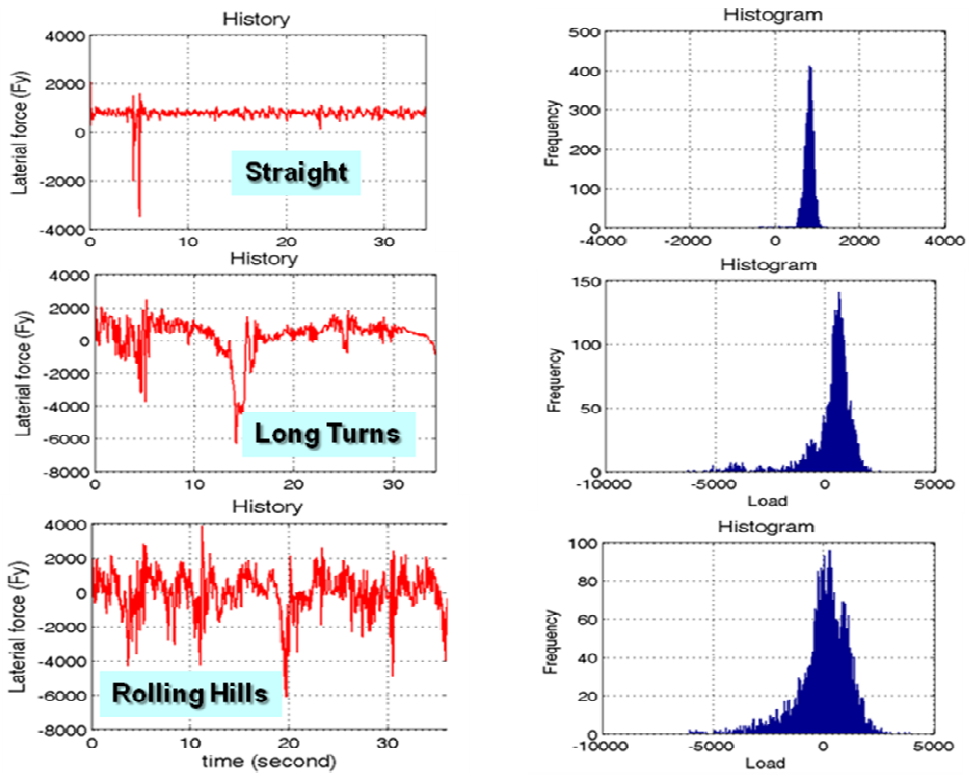

Figure 17 Joint Force Variations (Histories and PDF) in the LCA Ball Joint for Straight Road (upper), Horizontally Curved Road – Long Turns (middle) and Sloped and Curved Road – Rolling Hills (lower)

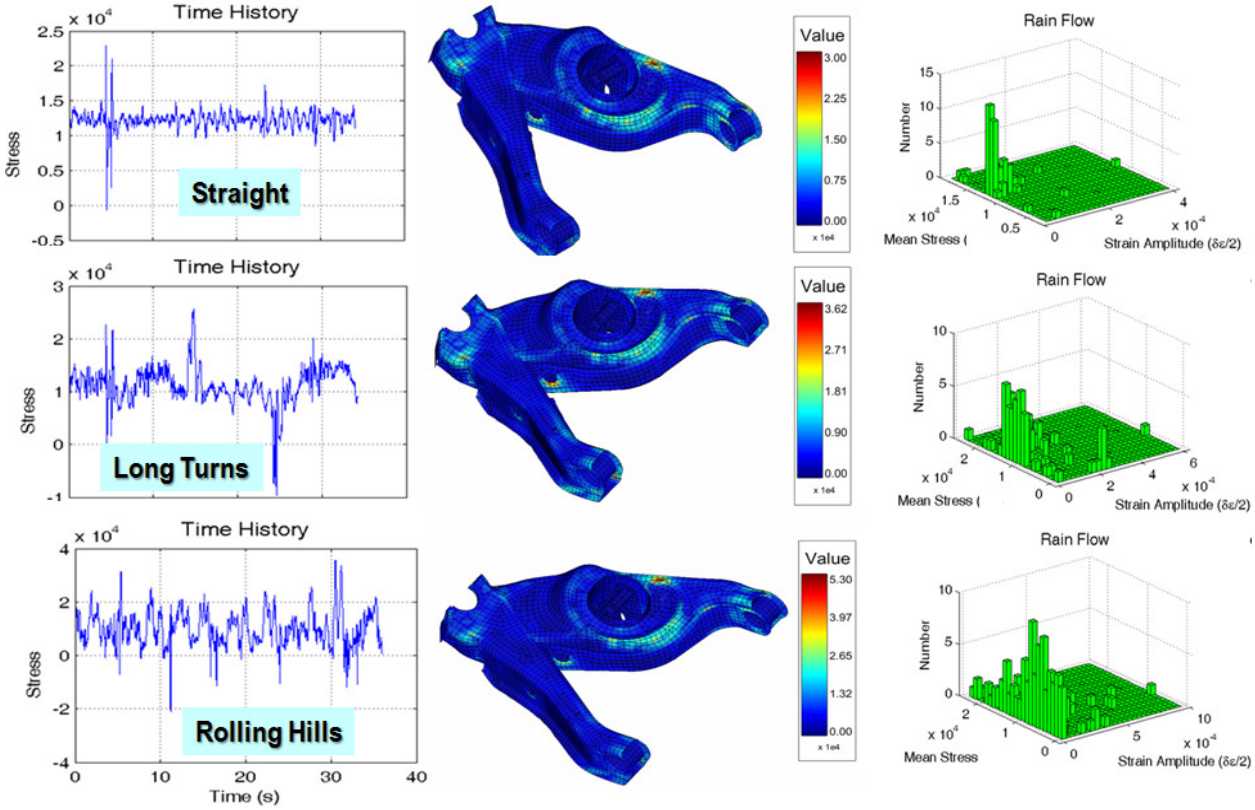

Figure 18 FLSS Stress at A Critical Location in LCA for Straight Road (upper), Horizontally Curved Road – Long Turns (middle) and Sloped and Curved Road – Rolling Hills (lower)

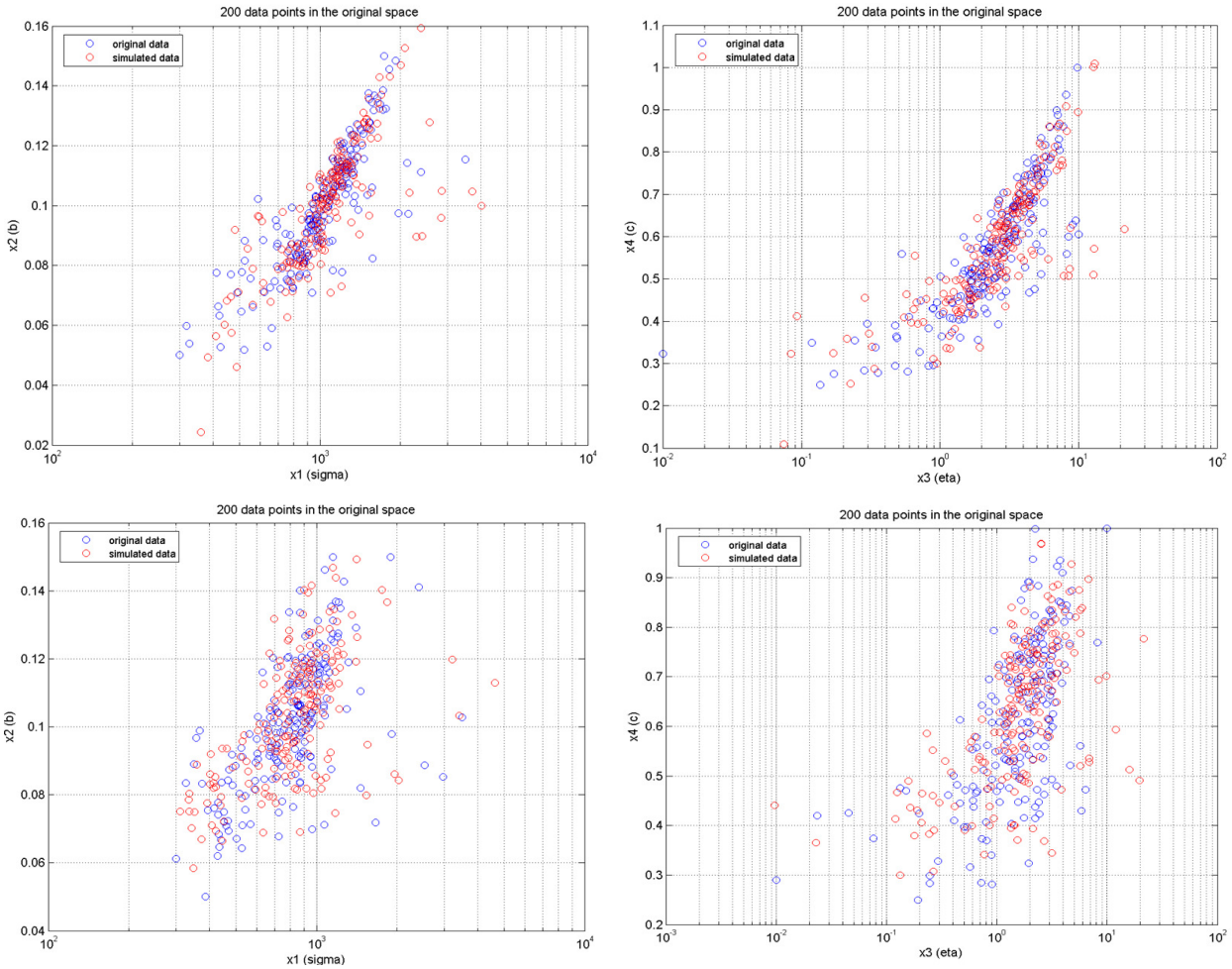

Figure 19 Strain-Life Parameter Data with High (Database A – upper plots) and Low (Database B –lower plots) Nonlinear Correlations; Shown for Parameter Pairs (b, Sigma) & (c, Epsilon)

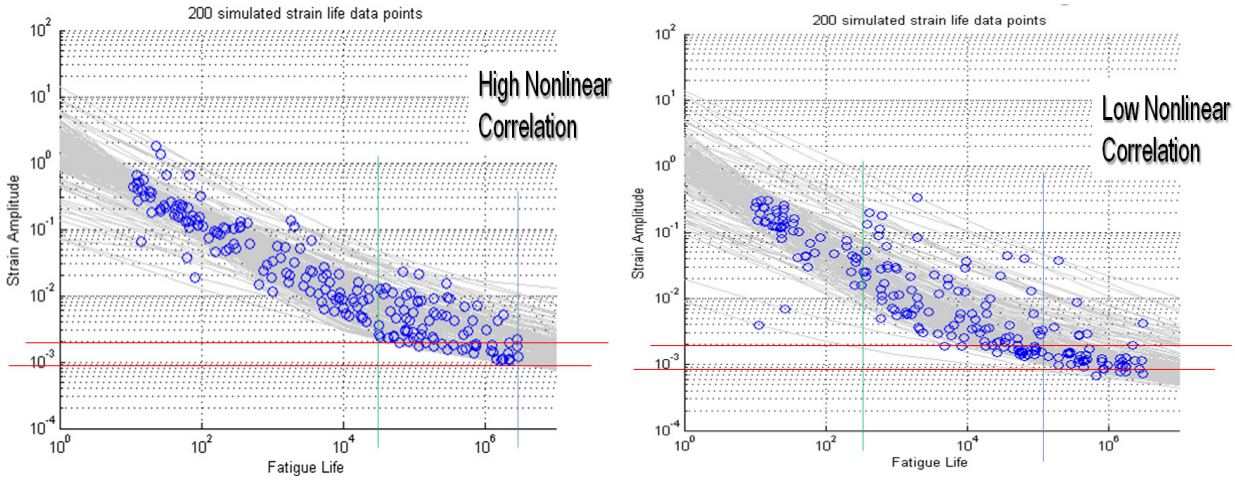

Database A Database B

Figure 20 Simulated Strain-Life Curve Including Nonlinear Correlation Between Parameters

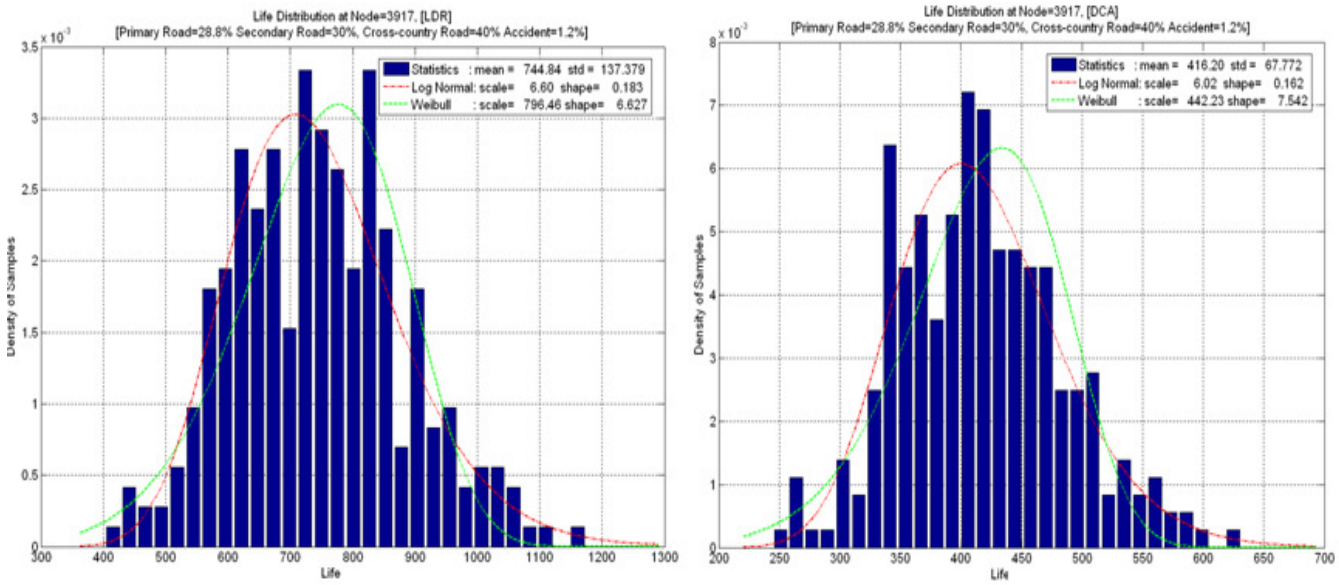

Figure 21 Predicted FLSS Life Usind LDR and DCA Progressive Damage Models

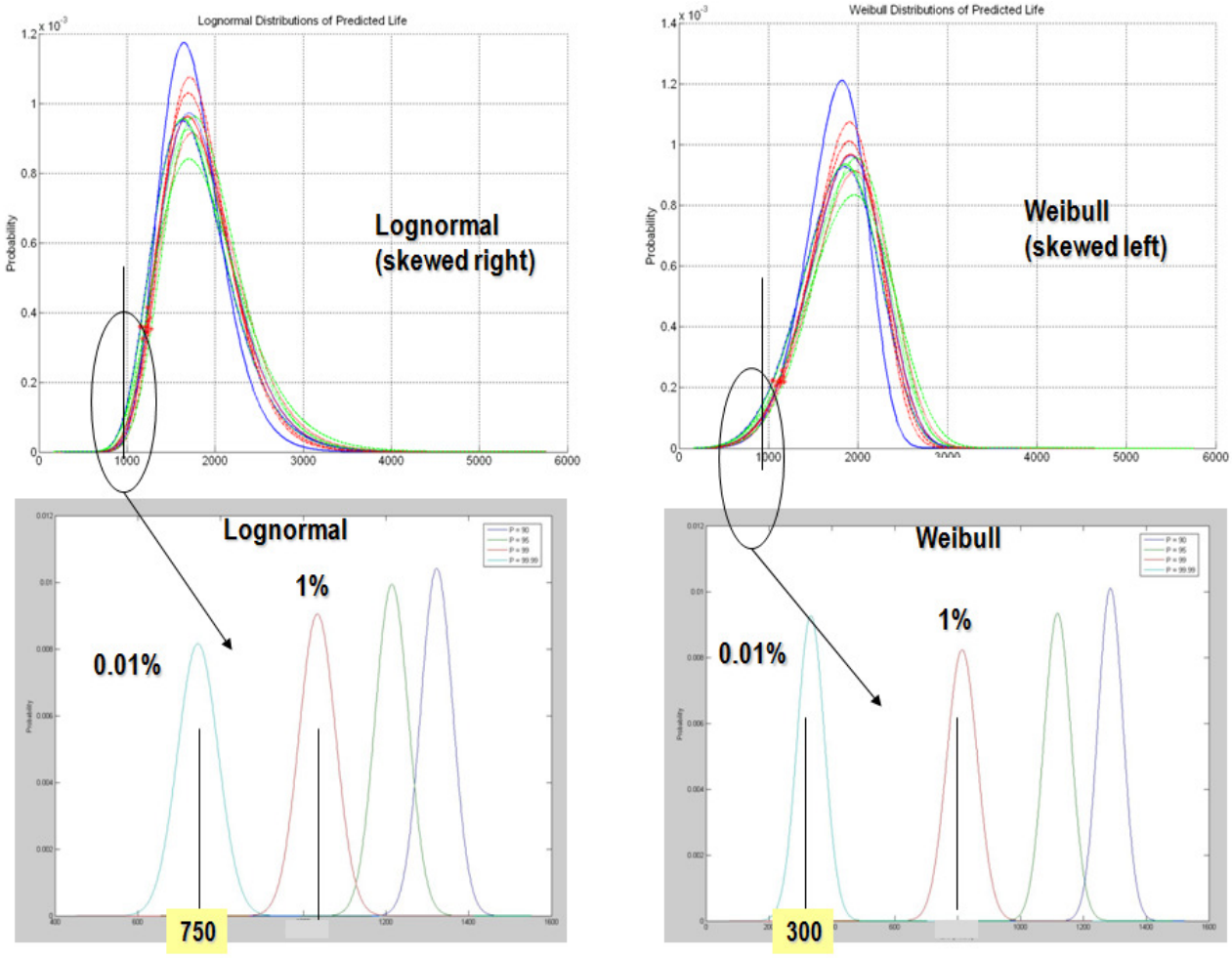

Figure 22 Effect of Lack of Data (280 Simulations) on Predicted Life for Given Reliability Levels of 90%, 95%, 99% and 99.99%

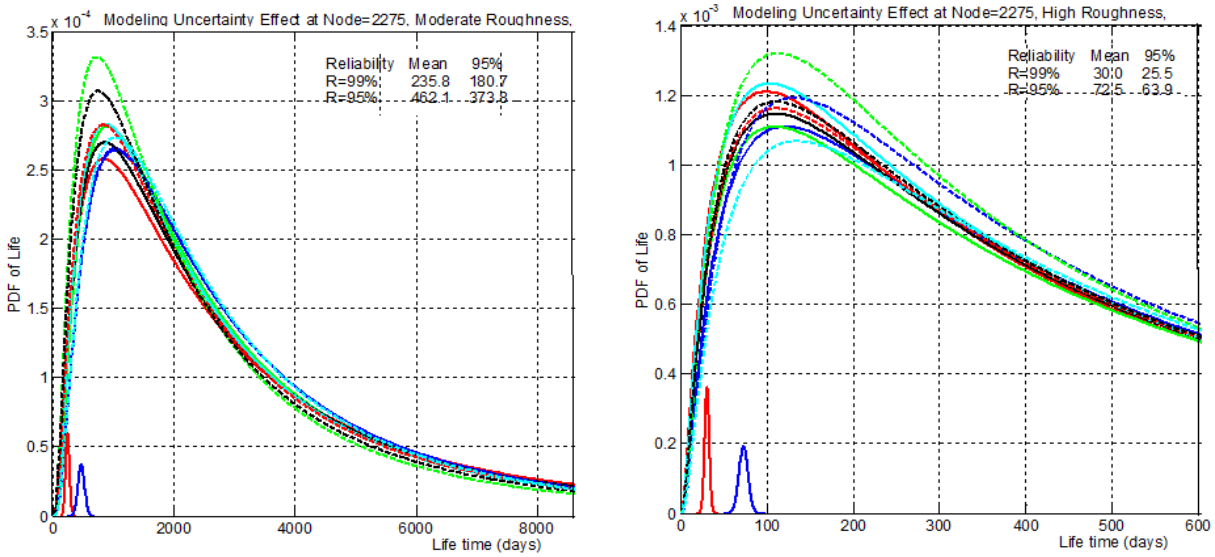

Figure 23 Model Uncertainty Effects on 99% & 95% Reliability Life for Moderate (left) and High (right) Roughness

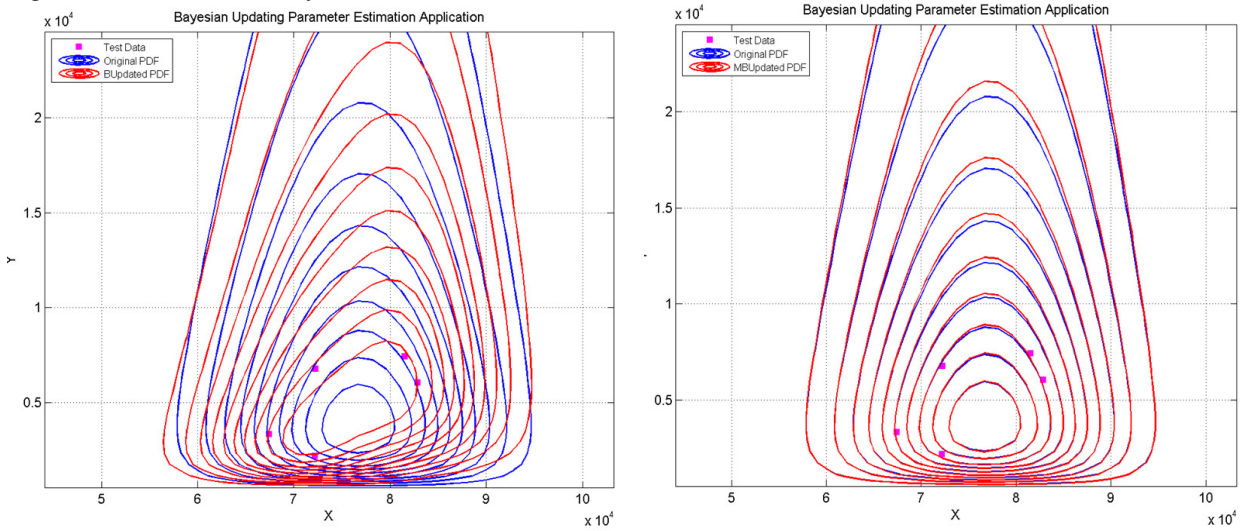

Figure 24 Prior & Posterior JPDF Using BU (left) versus BPT (right) for 5 Tests Assuming No Prediction Error

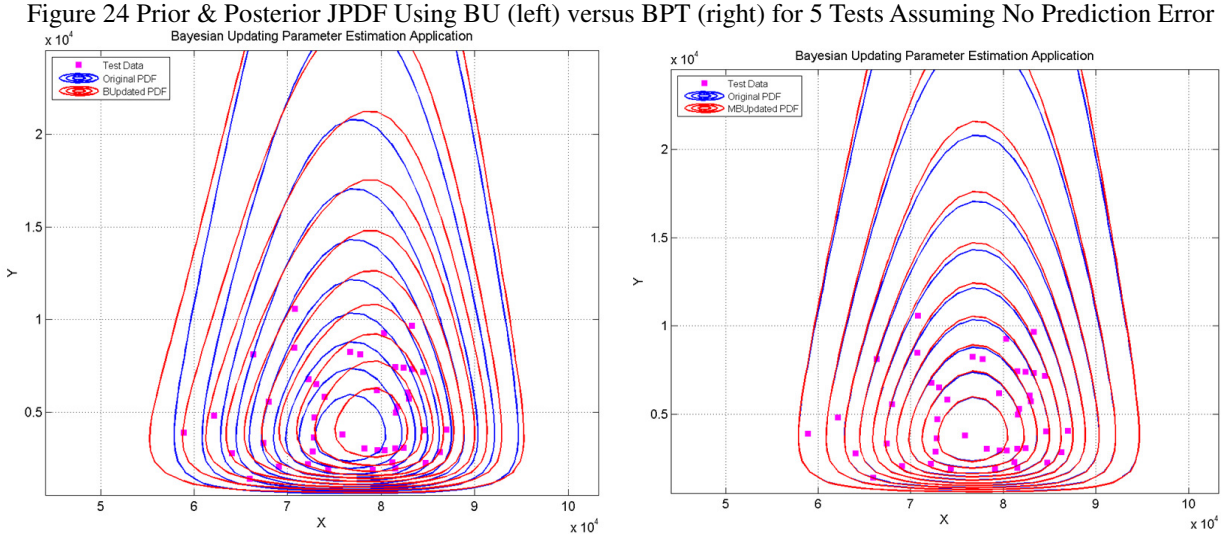

Figure 25 Prior & Posterior JPDF Using BU (left) versus BPT (right) for 25 Tests Assuming No Prediction Error

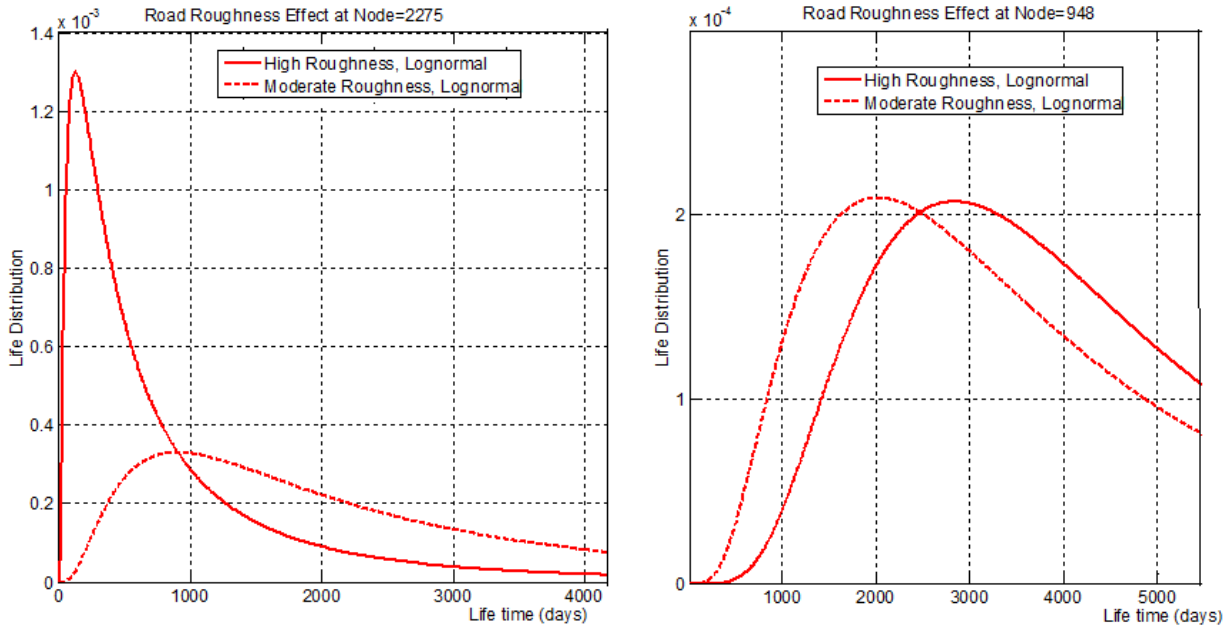

Figure 26 Effects of Road Surface Roughness on the Predicted Life PDF for the FLSS Governing Critical Location (left) and Other Critical Location (right); Both Critical Locations Are in the FLSS LCA Component

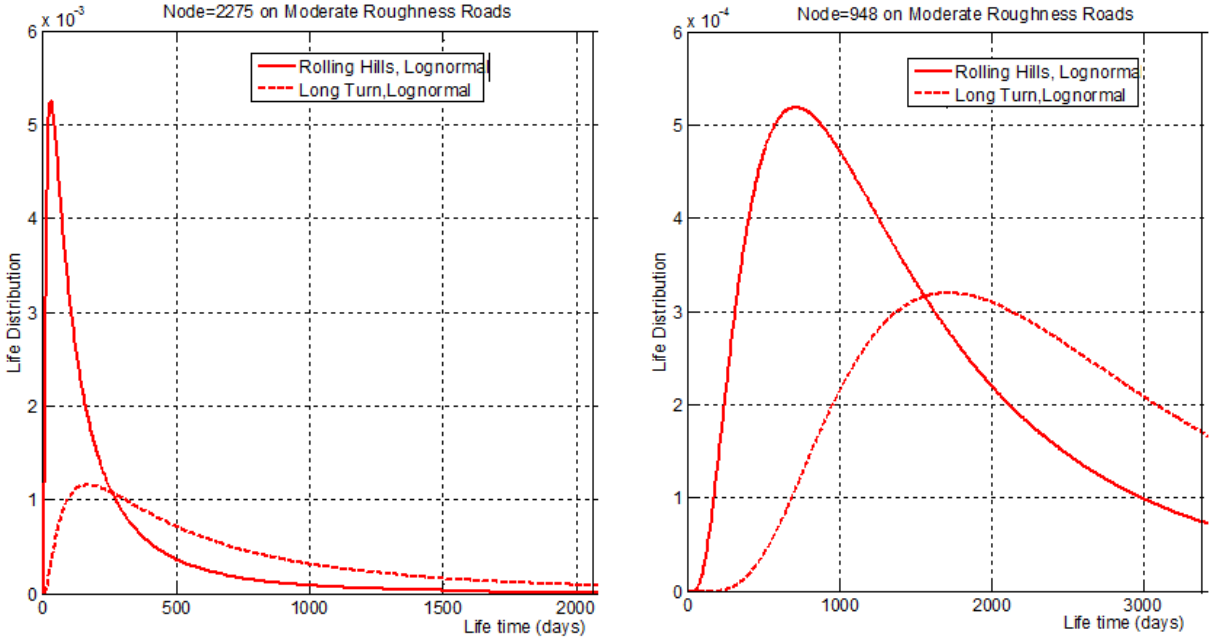

Figure 27 Effects of Road Topography on the Predicted Life PDF for the FLSS Governing Critical Location (left) and Other Critical Location (right) for Moderate Roughness; Both Critical Locations Are in FLSS LCA

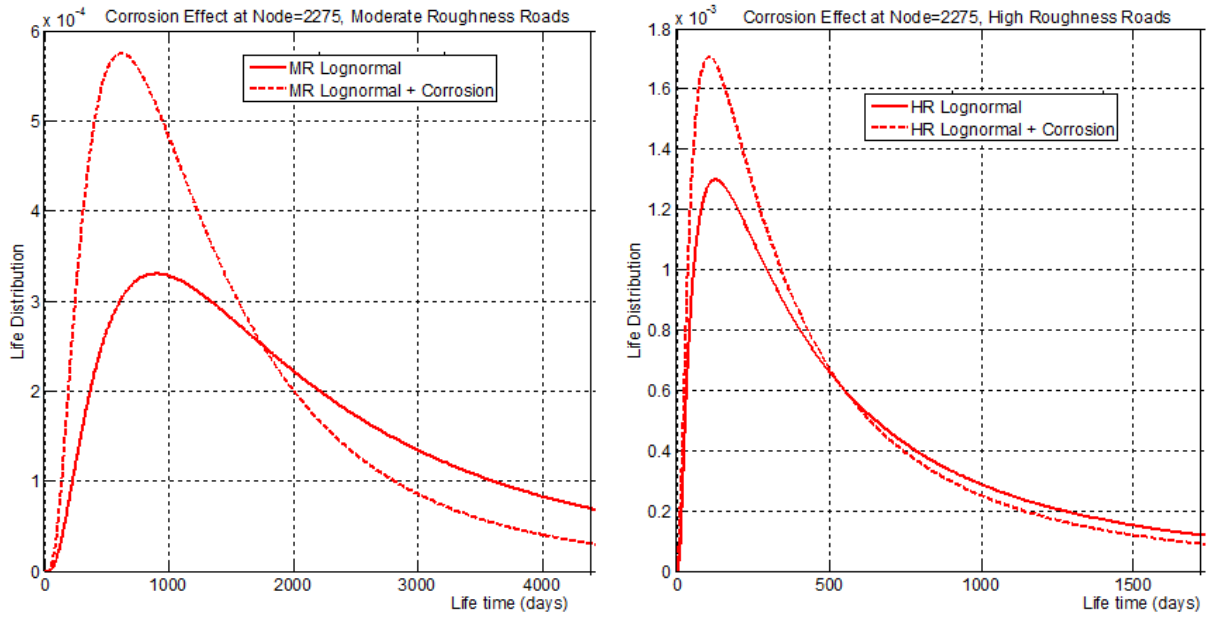

Figure 28 Effects of Corrosion on the Predicted Fatigue Life PDF for the FLSS Governing Critical Location for Moderate Road Surface Roughness (left) and High Road Surface Roughness (right)

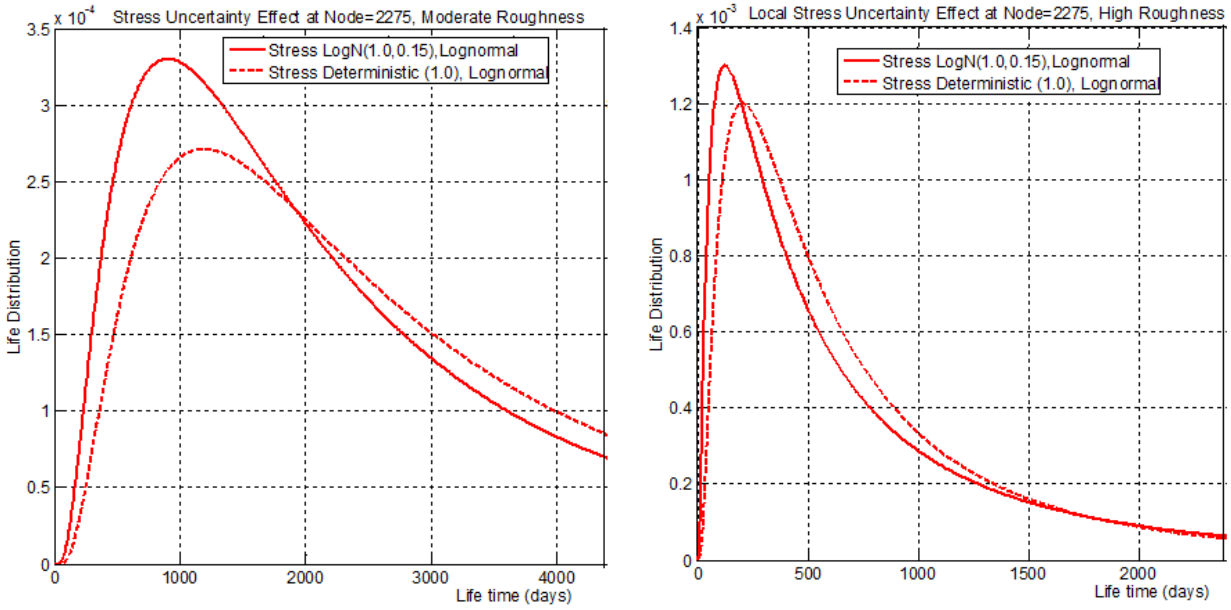

Figure 29 Effects of the FE Stress Prediction Uncertainty on the Predicted Fatigue Life PDF for the FLSS Governing Critical Location for Moderate Road Surface Roughness (left) and High Road Surface Roughness (right)

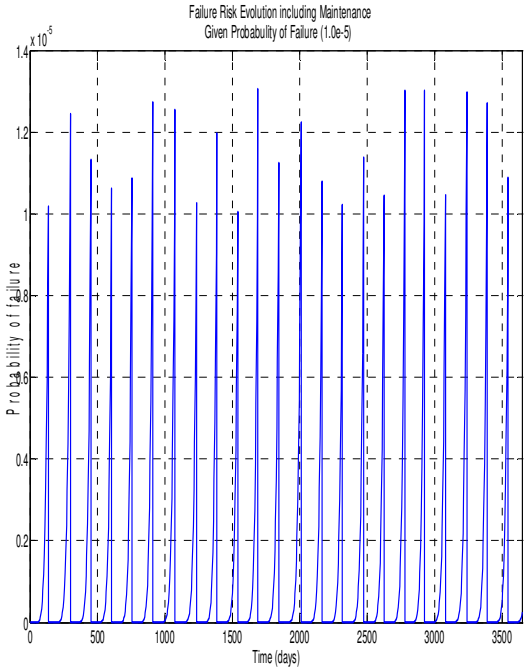

POF Variation for 1.0 E-05 Target POF

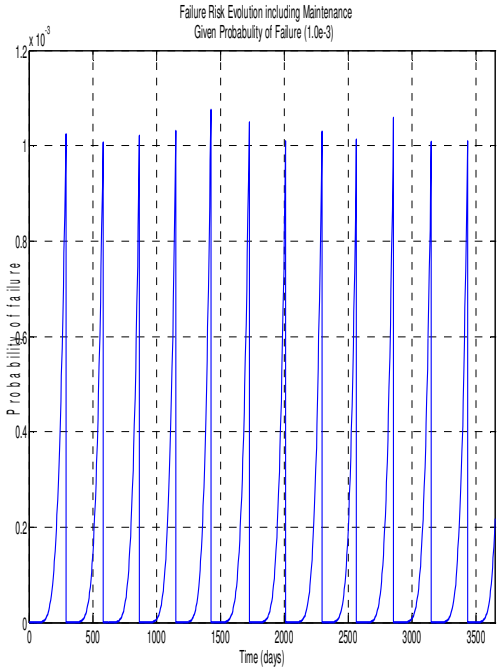

POF Variation for 1.0 E-05 Target POF

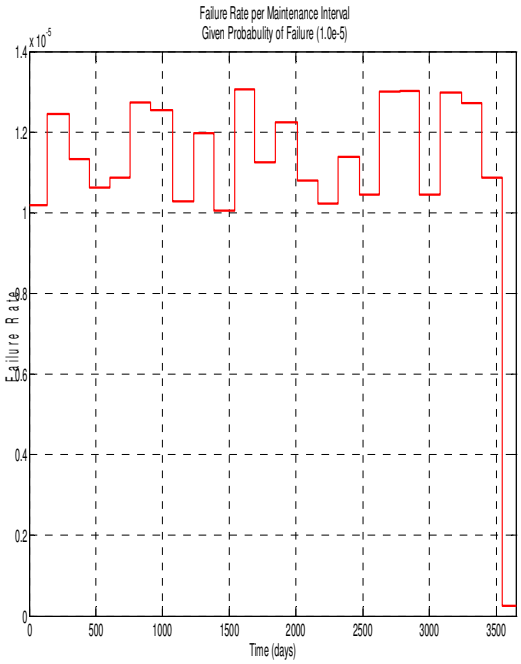

MHFR Variation for 1.0 E-05 Target POF

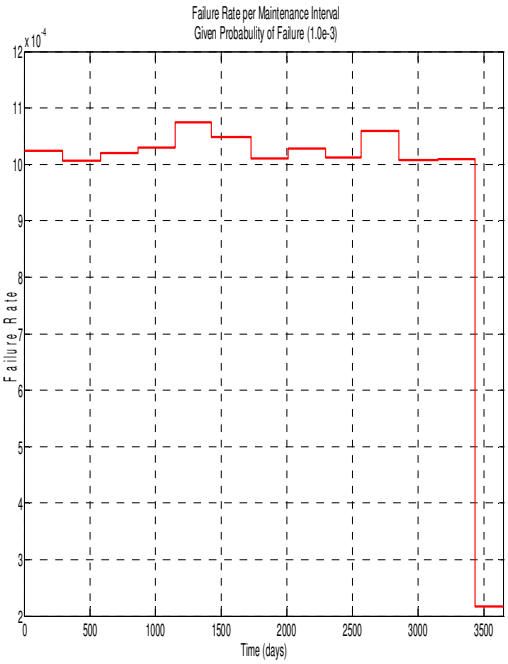

MHFR Variation for 1.0 E-05 Target POF

Figure 30 Computed Probability of Failure (POF – upper plots) and Mean Hazard Failure Rates (HFR – lower plots) Versus Time Given the Target Risks of 1.0 E-05 (left) and 1.0 E-03 (right)

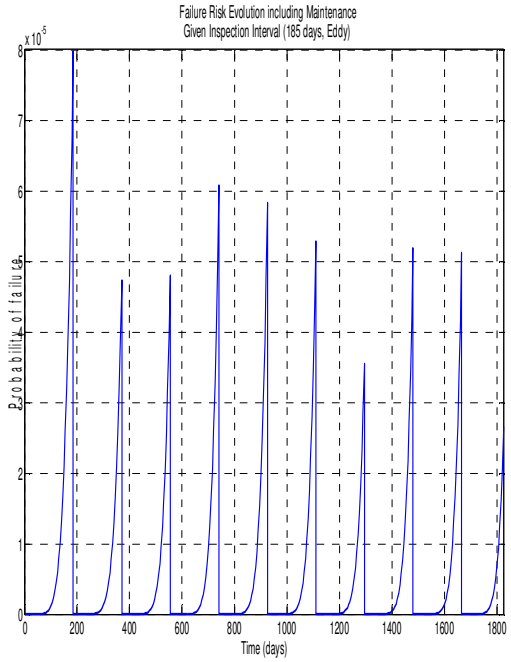

POF Variation for Eddy Current Inspection at 185 Days

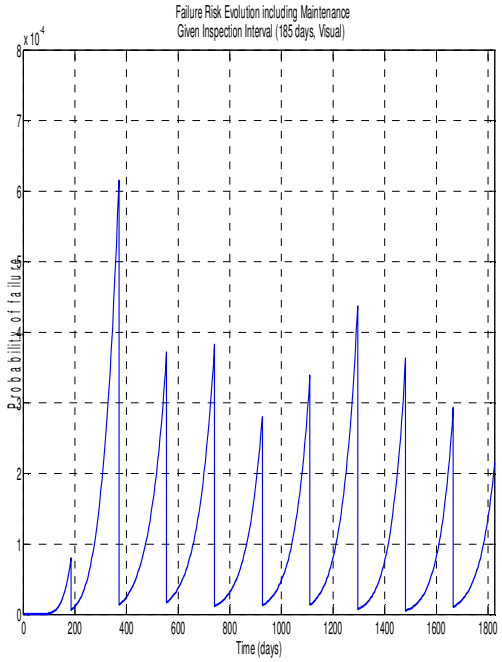

POF Variation for Visual Inspection at 185 Days

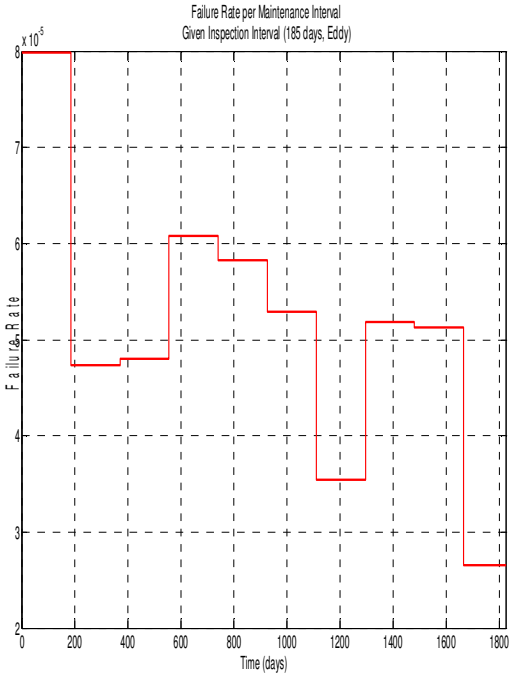

MHFR for Eddy Current Inspection at 185 Days

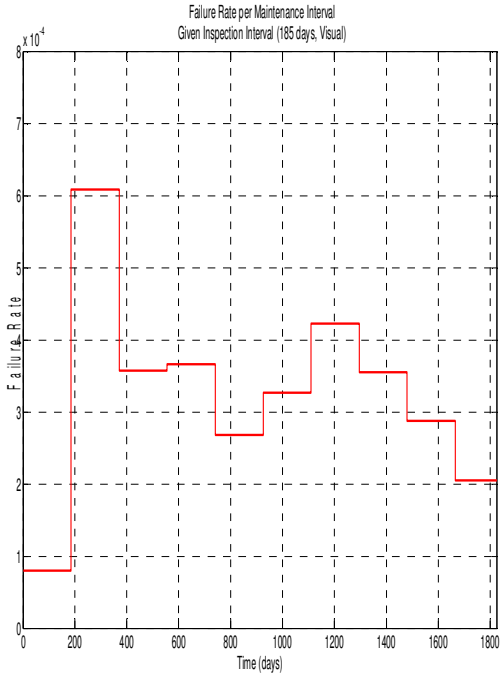

MHFR for Visual Inspection at 185 Days

Figure 31 Effects of Inspection Techniques on Computed Probability of Failure (POF – upper plots) and Mean Hazard Failure Rates (HFR – lower plots); Eddy Current (left) and Visual (right)

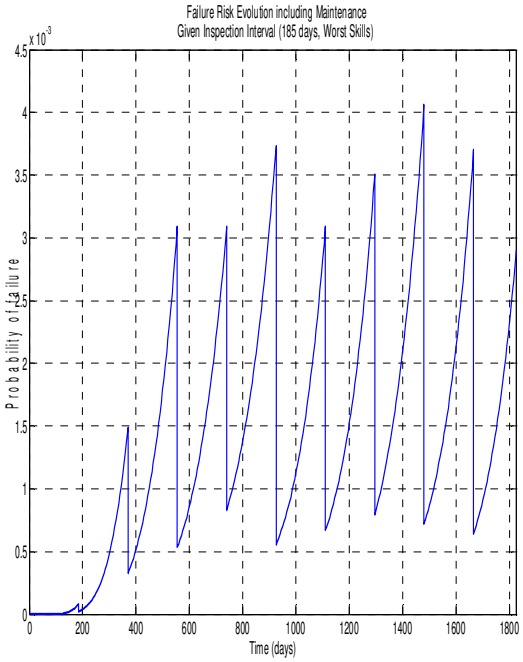

POF Variation for Edyy Current Worst Skill Operator

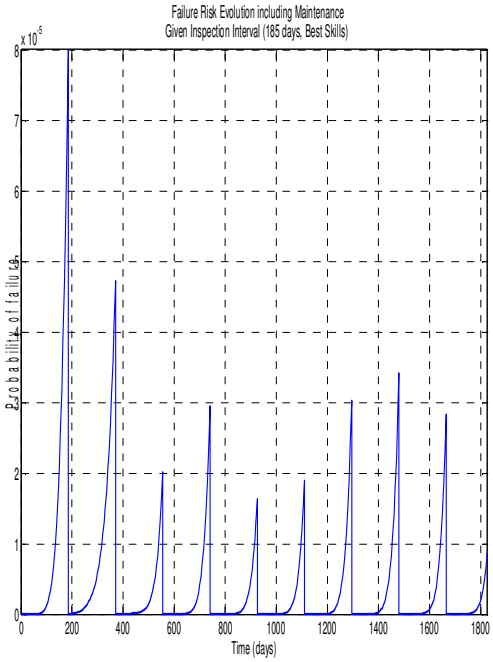

POF Variation for Edyy Current Best Skill Operator

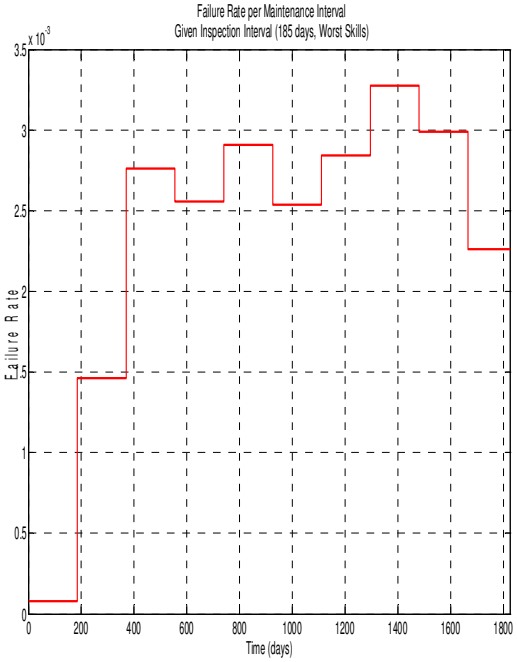

MHFR Variation for Edyy Current Worst Skill Operator

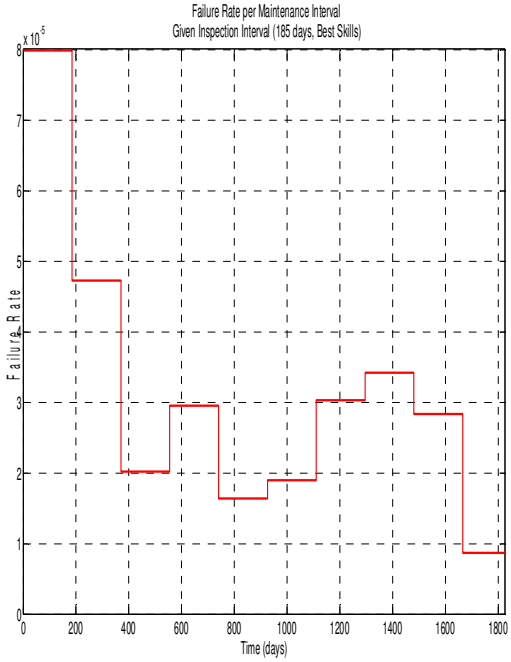

MHFR Variation for Edyy Current Best Skill Operator

Figure 32 Effects of Eddy Current Operator Skills on Computed Probability of Failure (POF – upper plots) and Mean Hazard Failure Rates (HFR – lower plots); Worst Skills (left) and Best Skills (right)

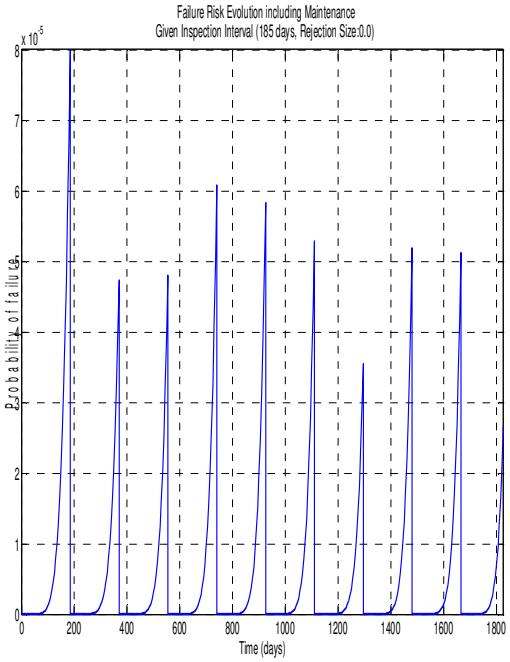

POF Variation for Crack Size Rejection Limit = 0.0 in

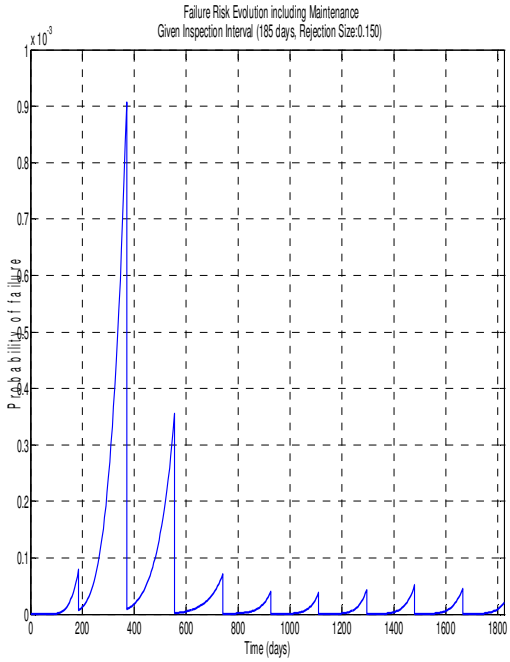

POF Variation for Crack Size Rejection Limit = 0.15 in

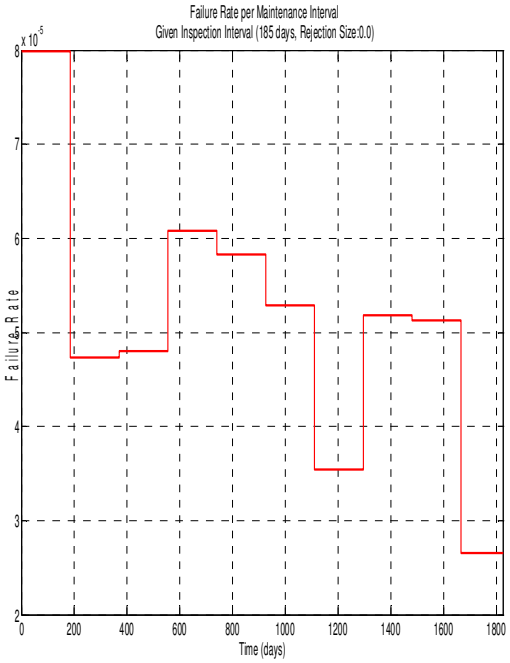

MHFR Variation for Crack Size Rejection Limit=0.0 in

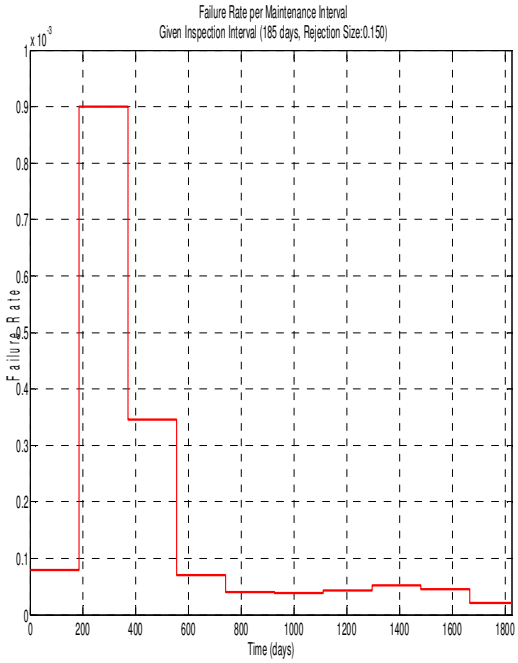

MHFR Variation for Crack Size Rejection Limit=0.15 in

Figure 33 Effects of Crack Size Rejection Limit on Computed Probability of Failure (POF – upper plots) and Mean Hazard Failure Rates (HFR – lower plots); Crack Size Limit = 0 (left) and Crack Size Limit = 0.15 in (right)